First principle study of the physical properties of actinide oxides. A review

Alexander Galashev [a] [*]
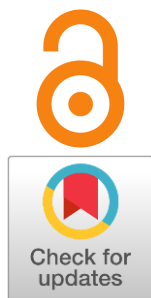
Reprocessing spent nuclear fuel creates the conditions for converting nuclear energy to a clean and sustainable energy. Thermal conductors in reactors are molten salts, the safe use of which is based on an accurate knowledge of their thermophysical properties. Due to the difficulty of experimentally measuring these properties, computational methods are coming to the fore. The main component of SNF is uranium dioxide, the change in the structure, energy and electronic properties of which when oxygen is removed from the system and plutonium is added to it was studied using DFT + U calculations. The influence of noble metals present in spent fuel on the process of direct reduction of irradiated nuclear fuel is considered. This work also examines the effects of doping thorium with uranium when Th-U fuel is used in a nuclear reactor. The paper presents data on the calculation of heat capacity, thermal conductivity, elastic moduli and phase transitions occurring in UO_2 at high pressures. The thermodynamic stability of actinide oxides is discussed in detail. The ways of improving DFT calculations to increase the accuracy of determining the properties of these nuclear materials are analyzed.

keywords: actinide oxides, electrochemical reduction, DFT calculations, noble metals, oxygen vacancies, spent nuclear fuel

1. Introduction

Currently, almost all of the energy generated by nuclear power plants worldwide is created mostly by "slow-neutron" reactors. These reactors use moderating materials that, through multiple collisions with the nuclei, slow down the fast neutrons emitted by fission. These slowed neutrons cause additional fission (Figure 1). The energy range over which fissionable nuclei can capture neutrons increases significantly at low neutron speeds [1]. Uranium-238 (^{238}U), which is typically non-fissile, captures most of the slow neutrons and becomes ^{239}Pu. In contrast, the fission of ^{235}U, which is two orders of magnitude less abundant than ^{238}U, produces new neutrons that sustain the chain reaction.

Currently, the energy resource uranium is used by nuclear reactors only in the amount of about 1 percent of the total energy value. Combining fast reactors with fuel recycling into a single complex creates the conditions for almost 100 % combustion of nuclear fuel, including not only uranium and actinides, but also long-lived fission products. Thus, spent nuclear fuel is no longer considered waste, but is perceived as a renewable resource that can be reprocessed into new nuclear fuel and valuable isotopes.

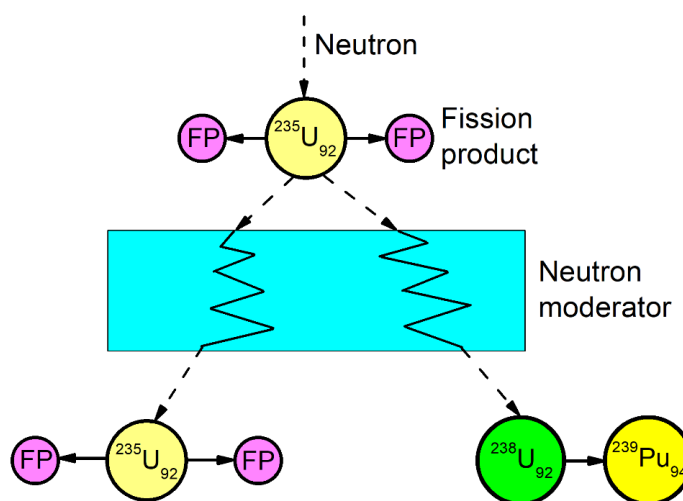

Figure 1 A fission chain reaction in a slow-neutron reactor.

a: Institute of High-Temperature Electrochemistry, Ural Branch of Russian Academy of Sciences, Yekaterinburg 620990, Russia

* Corresponding author: alexander-galashev@yandex.ru

The creation of a closed fuel cycle solves the problem of inefficient use of the energy potential of uranium raw materials [2, 3]. In this case, the full use of the potential of natural raw materials is achieved by involving ^{238}U in the cycle. The deferred problem with waste is also solved, since after processing the spent nuclear fuel, the obtained nuclear materials can be used again. The potential for biological-hazard waste is significantly reduced due to transmutation, or "after burning" of minor actinides in fast neutron reactors. The problem of non-proliferation of nuclear weapons is solved, since a fast reactor does not produce plutonium. In addition, it does not require enriched uranium at all.

ThO$_2$ is a good candidate for the pressurized water reactors (PWRs), as well as reactors using mixed oxide (MOX) fuel. Thorium itself is not a fissile element. Therefore, to carry out the nuclear fission reaction, external sources of neutrons are required, which can be uranium and plutonium. In the case of using thorium fuel, radioactive decay ceases as soon as the neutron source runs out. The use of thorium as a nuclear fuel prevents any reactor meltdowns. Such fuel may contain uranium impurities either as a result of deliberate addition of uranium to the thorium in MOX fuel or as an impurity.

Thermal reactors use natural or enriched uranium as fuel. Spent nuclear fuel (SNF), i.e. the fuel discharged from a nuclear reactor, contains many useful, albeit radioactive, products such as uranium, plutonium, and fission products such as ^{137}Cs and ^{90}Sr. Until now, SNF reprocessing has been carried out using the water method, i.e. using the so-called PUREX process (plutonium and uranium extraction). However, the pyrochemical method of SNF recovery using molten salt electrolysis is currently being intensively developed. High-level liquid waste from the PUREX process contains lanthanide fission products, other fission products and corrosion products of structural materials present in 3–4 M nitric acid medium. Their radioactivity is mainly caused by minor actinides that have a long lifetime, such as ^{244}Am ($t_{1/2} = 433$ years) and ^{244}Cm ($t_{1/2} = 18.1$ years), which generate alpha radiation.

The advantages of the pyrochemical method of SNF reprocessing over the aqueous method are expressed in the possibility of handling spent fuel with a high degree of burnup, the compactness of the equipment used, the reduction of the criticality of the accident, the formation of minimal aqueous waste for reprocessing. Various actinides and fission products have different thermodynamic stability in a molten salt medium. The salt medium is the eutectic of chloride salts of alkali and alkaline earth metals. The composition of the eutectic

determines the operating temperature of the electrolytic method of SNF extraction. Analysis of spent nuclear fuel of the high dose-rate turns out to be very demanding, labor-intensive and expensive [4]. An alternative technique to this is computer modeling.

In the nuclear fuel cycle, actinides are usually found in the form of an oxide (AnO$_2$) [5], which has higher thermal and chemical stability than the metal [6]. This form of nuclear fuel provides higher operating temperatures and protects it from further oxidation. This, in turn, limits the risk of rupture of the protective shell and thermal emission, improving the stability of the spent nuclear material for long-term storage [7]. In some cases, further oxidation of the fuel occurs when hyperoxides of the form AnO$_{2+x}$ are formed [8]. The lack of precise information on the fundamental properties of actinide oxides is due not only to radioactivity, but also [9] to their low content and isolation. The development of new strategies for processing and storage of nuclear material requires knowledge of the properties of these materials, such as lattice constant, bulk moduli, heat capacity, thermal conductivity, electronic conductivity and band gap. In the field of studying actinide oxides, the situation has now developed where the results of modern quato-mechanical calculations are better for predicting all the properties of these compounds than difficult-to-access and expensive experimental studies.

$5f$ electrons of actinide oxides experience strong Coulomb repulsion, i.e. they are excessively delocalized due to strong correlation. Both the local density approximation (LDA) and the generalized gradient approximation (GGA) fail to describe correctly the interaction between $5f$ electrons in actinide oxides. However, introducing the Hubbard correction "U" [10, 11], i.e. performing calculations in the LDA + U or GGA + U approximation, allows us to correctly reproduce the electronic structure of UO$_2$ and PuO$_2$ [12–14].

In [15], using DFT + U calculations, it was found that the introduction of Pu atoms into UO$_2$ leads to a narrowing of the band gap, and with a Pu content of 12.5 % in MOX, the band gap decreases from 2.4 eV (UO$_2$) to 1.5 eV. In work [16], using the quantum molecular dynamics (QMD) method, the melting temperatures T_m of MOX fuel were calculated depending on the concentration x of Pu in it. A local minimum of T_m was found at $x = 0.7$, where $T_m = 3050$ K. This value is slightly higher than the value $T_m = 2975$ K obtained using the Calphad methodology [17]. The authors of the work [16] were unable to explain the nature of this discrepancy.

The heat exchange between the fuel pellet and the cladding and the temperature distribution inside the pellet is determined by the thermal conductivity of the

nuclear fuel, i.e. UO$_2$ in the case of thermal reactors. The thermal conductivity of UO$_2$ of different isotopic compositions (by U) was studied using first-principles DFT calculations without taking into account the Hubbard correction (a correction introduced because of strong 5f electron correlations) in [18]. The calculations were performed with ^{235}U concentrations of 3 %, 5 %, 7 %, and 20 %. It was found that the thermal conductivity of the mixed isotopic dioxide decreases with increasing impurity level. At a temperature of 300 K, the largest contribution to the thermal conductivity is made by acoustic transverse (TA) phonons, while the contribution of optical branches to the total conductivity is small.

Elastic constants provide an idea of the mechanical properties of a solid and characterize its thermodynamic stability. In [19], it was shown that spin orbit coupling (SOC) does not significantly affect the values of elastic constants of a cubic crystal formed by oxides of heavy elements. Each elastic constant characterizes the mechanical response to a certain type of deformation. For example, in the case of a cubic crystal, C_{11} determines the resistance to compression along the main crystallographic axis, while C_{44} reflects the resistance to shear deformation across the (100) plane in the [010] direction. Elastic moduli are directly related to macroscopic distortions of the crystal structure, as well as to the assessment of elastic energies or deformations in materials.

The small energy gap between the 5f, 6d, and 7s orbitals creates the opportunity for variable oxidation states of actinides. The maximum oxidation state increases from +4 for Th to +7 for Np, but then decreases further through the series. UO$_2$ is the most common fuel for thermal reactors. The most stable states of uranium in combination with oxygen are U^{4+}, U^{5+} and U^{6+}. However, less stable uranium oxides such as U$_4$O$_9$, U$_3$O$_7$, U$_2$O$_5$, U$_3$O$_8$, UO$_3$ are also observed, data on which are still scarce [20]. In the actinide series of elements, each added electron goes into the orbital of the fifth shell, forming an orbital designated as 5f. The 5f orbitals in actinides that are more distant from the atomic nucleus create more variable valences (number of electrons available for chemical bonds) than in lanthanides, where the 4f orbitals are being filled.

Quantum mechanical DFT calculations of thermal conductivity, heat capacity, elastic moduli, density or lattice constant of UO$_2$, PuO$_2$, and actinide oxides allow one to extract knowledge that is difficult to obtain experimentally. In this review, in addition to these data, considerable attention is paid to DFT calculations related to electrolytic reprocessing SNF, including determination of the electronic properties of actinide oxides. The purpose of this review is to initiate DFT calculations to obtain new data on the properties of actinide oxides that are so necessary for the development and implementation of closed nuclear fuel cycle technology on an industrial scale.

2. Materials and methods

Metals (Ag, Pd, Pt, Rh, Ru, Te, Tc, Sb, Cd, In and Sn) with higher oxygen potential than UO$_2$ containing some Pu are present in SNF. These metal inclusions affect the SNF reprocessing process. DFT + U calculations related to the determination of the properties of uranium oxides of hypostochiometry and noble metal-containing oxides were performed using the SIESTA code package. The exchange-correlation relationship was represented using the LDA approximation. Systems of two sizes were investigated. In one case, the uranium dioxide model was represented by a 2 × 2 × 2 face-centered cubic uranium lattice (8 uranium atoms), in which two cubic oxygen cells (16 oxygen atoms) were inserted [21, 22]. A system with full stoichiometry, as well as systems with two and four oxygen atoms removed, were investigated. The inclusion of plutonium (or noble metal) was carried out by replacing one or two U atoms with Pu or one U atom per noble metal atom Me (Ag, Au, Pd, Pt) [21, 22]. In the case of replacing one U atom, a Pu/U or Pu/Me ratio in the considered structures was 1 : 7 and when two U atoms were replaced, the Pu/U ratio was 1 : 3. In the second case, when studying uranium oxides containing noble metals, the size of the system was increased. These systems contained 15 uranium atoms, 1 noble metal atom, and 32 oxygen atoms. The calculations with the expanded system allowed us to estimate the influence of noble metal concentration on the electronic structure of the oxide compounds. Taking into account the strong correlation between f electrons in the model was considered in [23]. The Hubbard corrections U_H and J_H for uranium atoms used in [21, 22] had values of 4.5 and 0.5 eV, respectively. For plutonium atoms, these corrections were 10 and 0 eV, respectively. In [21, 22], the Brillouin zone was determined using the Monkhorst-Pack method [24], while a 5 × 5 × 5 grid was used. All geometry was fully optimized based on the local density approximation in the form of Ceperley-Alder (CA) [25]. Control over the calculation of electron density was carried out by choosing a cut-off energy of 550 Ry. Periodic Born-Karman boundary conditions were used.
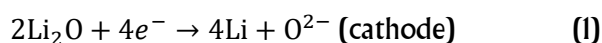
Thorium oxide has advantages over traditional nuclear fuels (UO$_2$ and PuO$_2$) in terms of safety, waste generation and availability. Currently, developments in the study of the use of thorium as a nuclear fuel continue. An example of a DFT study of the properties of thorium fuel is the work [26]. To simulate ThO$_2$, which has a

fluorite structure, $1 \times 1 \times 2$ and $2 \times 2 \times 2$ supercells containing 24 and 96 atoms, respectively, were used [26]. Calculations were performed using VASP. The exchange correlation interaction was represented by the functional of Perdew, Burke, and Ernzerhof (PBE) [27]. The projector augmented wave (PAW) method [28, 29] to describe the core electrons and the interaction between the atomic cores and the electrons in the valence shells were also used. The use of ultra-soft or PAW pseudopotentials can significantly reduce the energy cutoff when modeling with VASP. The plane wave basis set expansion was achieved due to a kinetic energy cut-off of 44 Ry. Convergence was ensured by using a gamma-centered Monkhorst-Pack k-points mesh of $6 \times 6 \times 6$. When using the (GGA + U), a decrease in hybridization with oxygen atoms and a weakening of the strong Coulomb repulsion arising from the presence of f-electrons in actinides is achieved using a correction to the Hamiltonian determined by the difference in the U_H and J_H parameters [22]. Calculations in [26] were performed using an effective correction $U_{eff} = U_H - J_H$ equal to 4 eV. Other authors, whose works are reflected in this review, used models similar to or differing in some known approximations from those described above. These models are most fully presented in the original works, references to which are given in the bibliography for this review.

3. DFT calculations of physical properties of actinide oxides

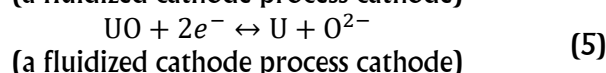### 3.1. The electronic properties of $U_xPu_yO_z$ compounds formed during the recovery of spent nuclear fuel

The displacement of uranium by lithium (Equations (1) and (2)) and direct reduction (3) underlie the electrochemical reduction of UO_2 in the molten salt LiCl + (1–3 %) Li_2O [30]. Direct reduction (Equation (3)) lags behind the reduction described by chemical Reactions (1) and (2). Reaction (3) occurs when the conducting phase has already been formed by removing oxygen from the material placed in the cathode basket (Equations (1) and (2)).

$$2Li_2O + 4e^- \rightarrow 4Li + O^{2-} \text{ (cathode)} \qquad (1)$$

$$4Li + UO_2 \rightarrow 2Li_2O \text{ (cathode)} \qquad (2)$$

$$UO_2 + 4e^- \rightarrow U \text{ (cathode)} \qquad (3)$$

The difficulty in maintaining direct reduction is the small difference (70 mV) in the potentials that give Reactions (3) and (1). Lithium, which is formed as a result

of Reaction (1), is used for the reduction of UO_2 (Reaction (2)).

A wider potential range in which Reactions (1)–(3) can occur, including the possibility of a two-electron transfer process, is achieved by using a fluidized cathode process, enhancing the transport of oxygen ions within the electrolyte [31]. In this case, two sequential reactions replace the reaction described by Equation (3):

$$UO_2 + 2e^- \leftrightarrow UO + O^{2-}$$
(a fluidized cathode process cathode) $\qquad (4)$

$$UO + 2e^- \leftrightarrow U + O^{2-}$$
(a fluidized cathode process cathode) $\qquad (5)$

Uranium forms thermodynamically stable compounds with oxygen. The best known of these are dioxide UO_2, triuranium octoxide U_3O_8, and trioxide UO_3. In addition, four more non-stoichiometric compounds of uranium with oxygen have been found: UO, U_2O_5, U_3O_7, and U_4O_9 [32].

The potential energy of interaction between the U and O atoms in the UO molecule was determined in the harmonic and anharmonic approximation using DFT calculations in [33] (Figure 2). The potential energy functions calculated in these approximations differ slightly, which is due to the smallness of the anharmonicity effect for the fundamental of stretching UO modes.
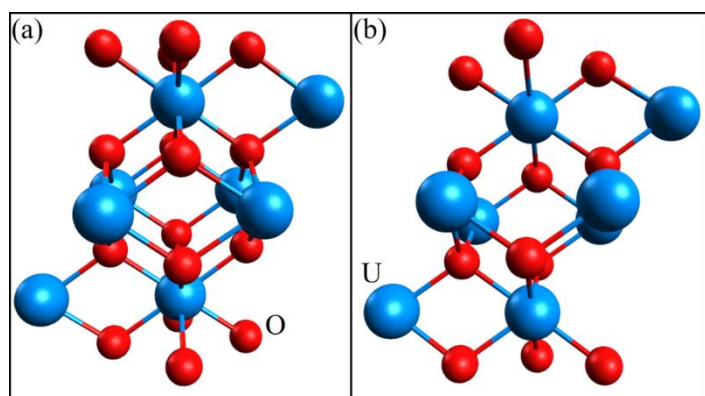
After removing portions of oxygen, as well as replacing some U atoms with Pu atoms, and performing dynamic optimization, the authors of [22] found that the U-U and Pu-U bond lengths in all the compounds considered were approximately 3.81 and 3.79 Å, respectively. Similar displacements of uranium atoms were observed in hypostoichiometric compounds UO_{2-x} [34].
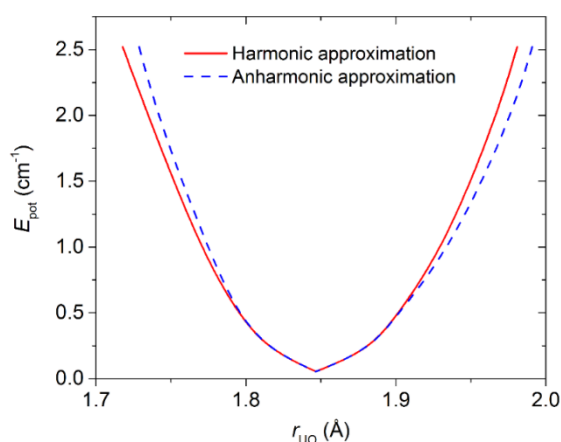
Figure 2 Potential energy functions of the interaction between uranium and oxygen atoms in the UO molecule, that calculated in harmonic and anharmonic approximations near equilibrium [33].

The geometric structures of the UO_2 and U_2O_3 systems obtained after geometric optimization are shown in Figure 3. As can be seen from the figure, the removal of 4 oxygen atoms from the UO_2 system did not lead to significant structural changes in the part of the system remaining after this act, which is due to the high stability of the framework formed by the U atoms.

The band structures of the resulting $U_xPu_yO_z$ systems are shown in Figure 4 [22]. In the case of uranium dioxide, the band gap was 2.23 eV, which slightly exceeds the similar characteristic (2.19 eV) obtained in [35].

After removing two oxygen atoms, the band gap narrows to 0.99 eV, and when 4 O atoms are removed, uranium oxide U_2O_3 becomes conductive. The narrowing of the band gap when uranium dioxide loses oxygen atoms and the gradual transition to the conducting state with a decrease in the oxygen content in the compound is consistent with the data from [34]. After replacing one and two uranium atoms with plutonium atoms, the compounds in question, acquire metallic conductivity, with the exception of the U_7PuO_{16} and U_7PuO_{14} systems.

The partial density of states (PDOS) for some of the systems studied in [22] can be observed in Figure 5. The Fermi energy is represented in Figure 5 by a vertical dashed line that denotes the zero energy value. The interactions of the d- and f-orbitals of uranium with the p-orbitals of oxygen lead to the compound U_2O_3 becoming conductive. The interactions of the $6d$-orbitals of uranium with the $5f$-orbitals of plutonium and the $5f$-orbitals of uranium and plutonium with the $2p$ orbitals of oxygen lead to conductivity in U_7PuO_{12} and $U_6Pu_2O_{16}$, respectively. Hybridization, leading to the formation of stronger covalent bonds, is carried out under the condition that the electron pairs are as far apart as possible.


Figure 3 Geometric structure of **(a)** UO_2 and **(b)** U_2O_3 after geometric optimization [22].
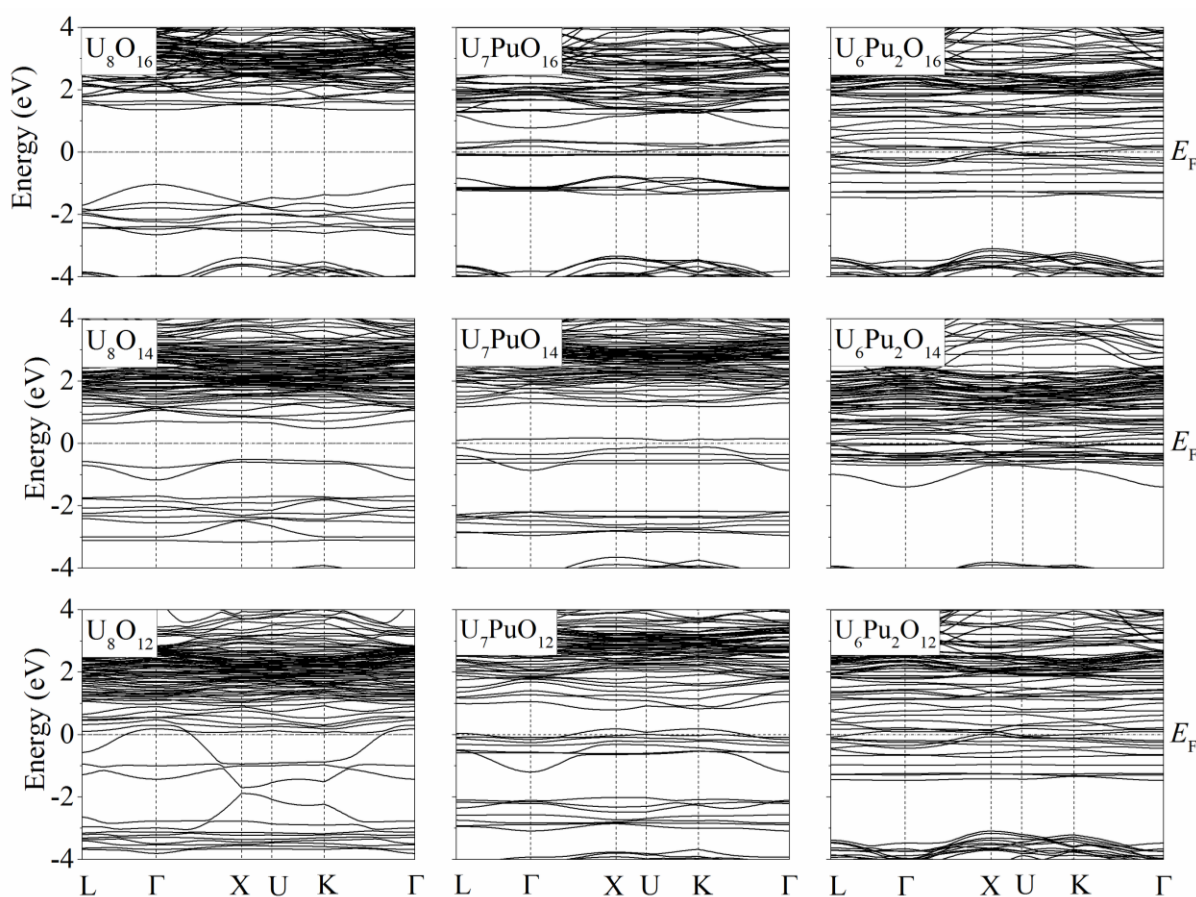
Figure 4 Band structures obtained for compounds U_8O_{16}, U_8O_{14}, U_8O_{12}, U_7PuO_{16}, U_7PuO_{14}, U_7PuO_{12}, $U_6Pu_2O_{16}$, $U_6Pu_2O_{14}$ and $U_6Pu_2O_{12}$ [22].
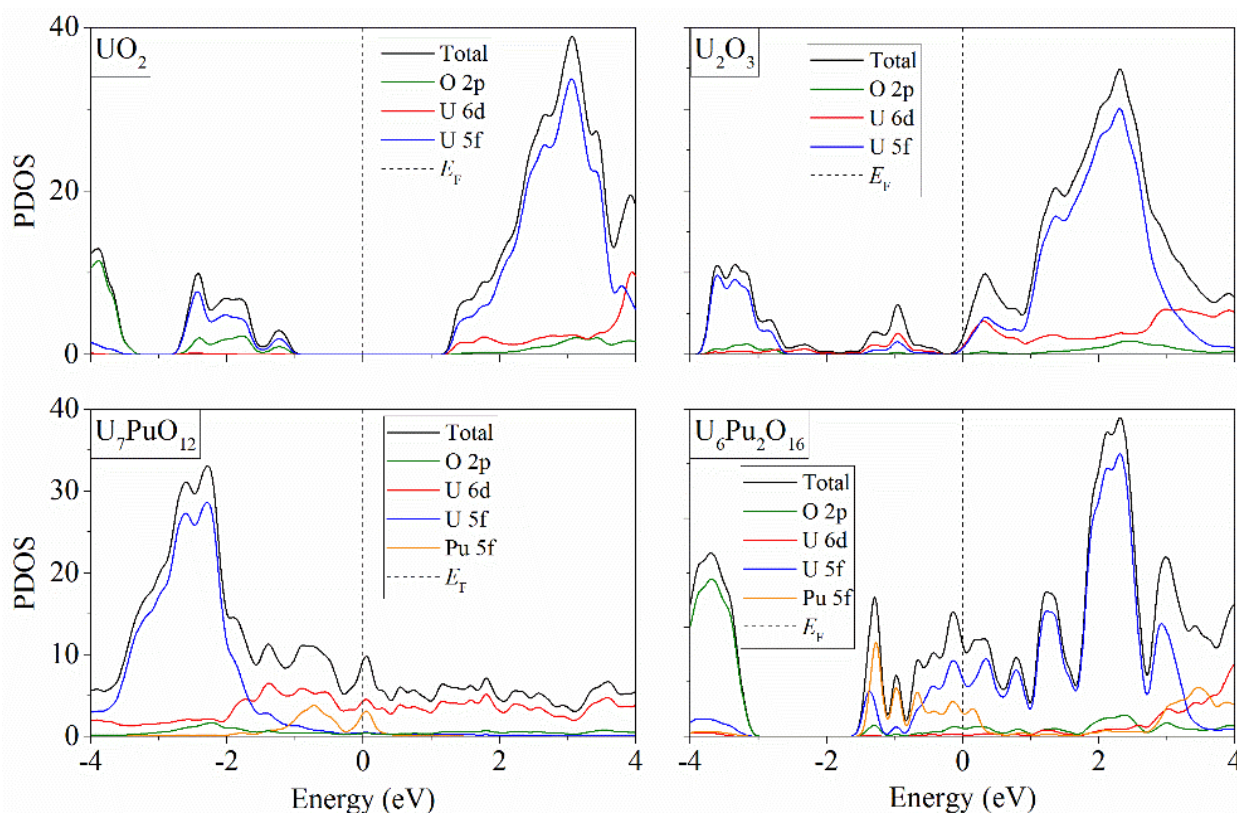
Figure 5 Partial density of electronic states obtained for compounds UO_2, U_2O_3, U_7PuO_{12} and $U_6Pu_2O_{16}$ [22].

The band gap **(BG)** of the hypostoichiometric compounds U_xO_y can be changed according to the amount of oxygen they contain, as shown in Figure 6. The location or sequence of oxygen atom removal from the system can cause different changes in BG, as has been found [22]. In the figure, there are two cases in which BG decreases monotonically with a decrease in oxygen in the system. Depending on the method of removing oxygen from the system, metallic conductivity may appear for different compositions, the limits of which are U_4O_5 and U_2O_3. The direct reduction of UO_2 according to Equation (3) is possible through the transition to the conducting state. Chemical (according to Equations (1) and (2)) and direct electrochemical reduction (3) take place simultaneously in the oxidized system. It is logical to assume that reduction with lithium first creates a conductive phase that can be eventually reduced through direct reduction.

The electrochemical method can lead to a UO_2 reduction rate of up to 99 %, which is a result of simultaneous chemical and direct reduction pathways [36–39]. The spent fuel that is not in contact with the electrolyte was analyzed by DFT + U calculations of electronic and geometric properties in [22]. Furthermore, the presence of Li^+ ions in the spent fuel during electrochemical reduction was not taken into account. Thus, an idealized system was used to investigate the dependence of SNF's geometric and electronic properties
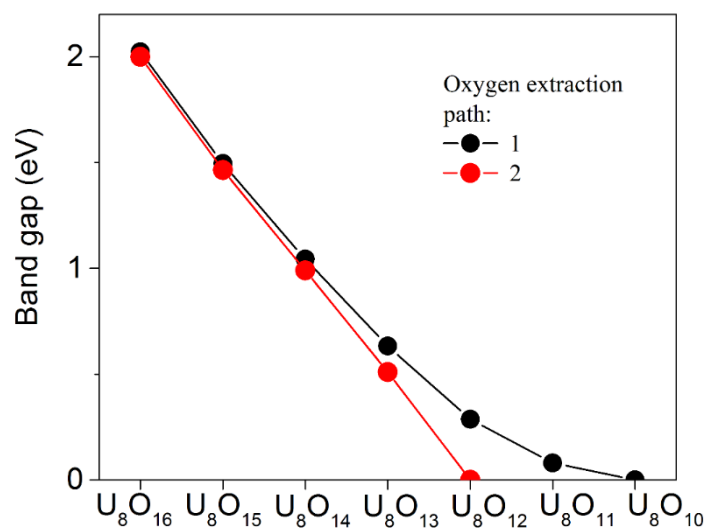
Figure 6 Band gap of "hypostoichiometric U_yO_x phases" [22].

on the concentration of oxygen vacancies. Quantitative information about the fuel properties obtained using DFT + U calculations improves the reliability and accuracy of the calculated material properties and also contributes to a better understanding of the microstructure of nuclear fuel. Improvements to existing DFT methods include the need to scale to a larger number of atoms, which will increase the accuracy of the prediction. Moreover, ab initio DFT calculations should be used to generate finite temperature predictions of material behavior.

3.2. The influence of noble metals on the process of reduction of uranium oxides

The noble metal phase formed in the irradiated nuclear fuel affects the process of spent fuel recovery. In [40], noble metals (Rh, Pd, Ir, Au) were used as O^{2-} releasing anodes during the electrolytic reduction of UO_2 in the molten salt LiCl-Li$_2$O. To some extent, this serves as experimental confirmation of the participation of noble metals in the process of UO_2 reduction. Au as an anode has been shown to have better electrochemical stability compared to Pt. Over time, an oxide layer appears on the platinum electrode in the form of Li$_2$PtO$_3$. However, local dissolution was still present in the newly used anodes. Inclusions of noble metals in spent fuel subject to recovery can act as catalytic electrodes [41].

It was experimentally shown that during electrochemical reduction in LiCl-Li$_2$O melts at 650 °C, uranium oxide is completely reduced to metal, while the lanthanide oxides La$_2$O$_3$, Nd$_2$O$_3$ and CeO$_2$ are not reduced [42]. However, when during electrochemical reduction palladium is added to the Nd$_2$O$_3$-CeO$_2$ oxide mixture, neodymium and cerium are almost completely reduced to the metallic state [43]. In [21], using DFT + U calculations, the recovery of defect-free (UO_2 compound) and defective (UO_2 compound with oxygen vacancies) uranium dioxide in the presence of substituting metal dopants (silver, gold, platinum, or palladium) was studied.

The geometric structures of uranium oxides having 16, 14 and 12 oxygen atoms when replacing one uranium atom with an Ag atom, obtained after geometric optimization, are shown in Figure 7 [21]. All the resulting structures appear as compact formations. The loss of oxygen atoms did not lead to the breaking of other U-O bonds, and the Ag atom replaced the U atom without significant lattice distortions.

The formation of electronic conductivity of a semiconductor is facilitated not only by the removal of oxygen but also by its doping with such noble metals as Ag and Au. This is reflected in the partial spectra of the electronic states of the compounds U$_7$AgO$_x$ and U$_7$AuO$_x$, where $x = 12, 14, 16$ (Figure 8). Electronic conductivity occurs due to the interaction of the $2p$ orbitals of oxygen with the 5f orbitals of uranium. As a rule, atomic orbitals whose energies do not differ very much take part in hybridization.
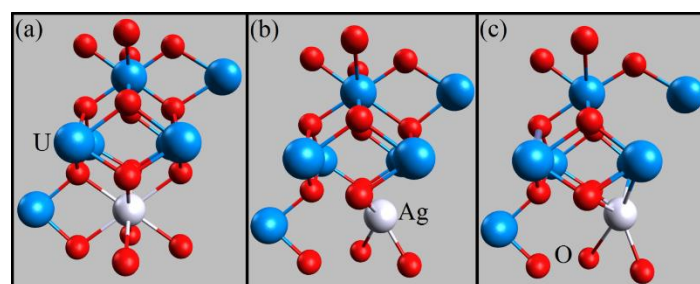
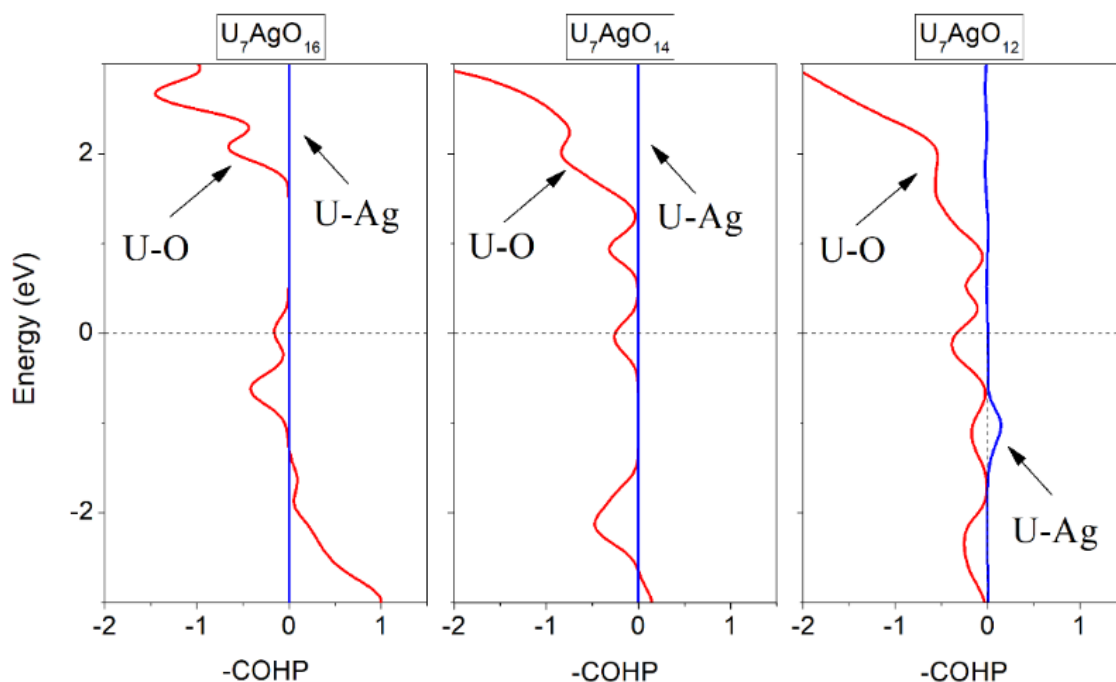**Figure 7** Structure of chemical compounds: (a) U$_7$AgO$_{16}$, (b) U$_7$AgO$_{14}$ and (c) U$_7$AgO$_{12}$ after geometric optimization [21].
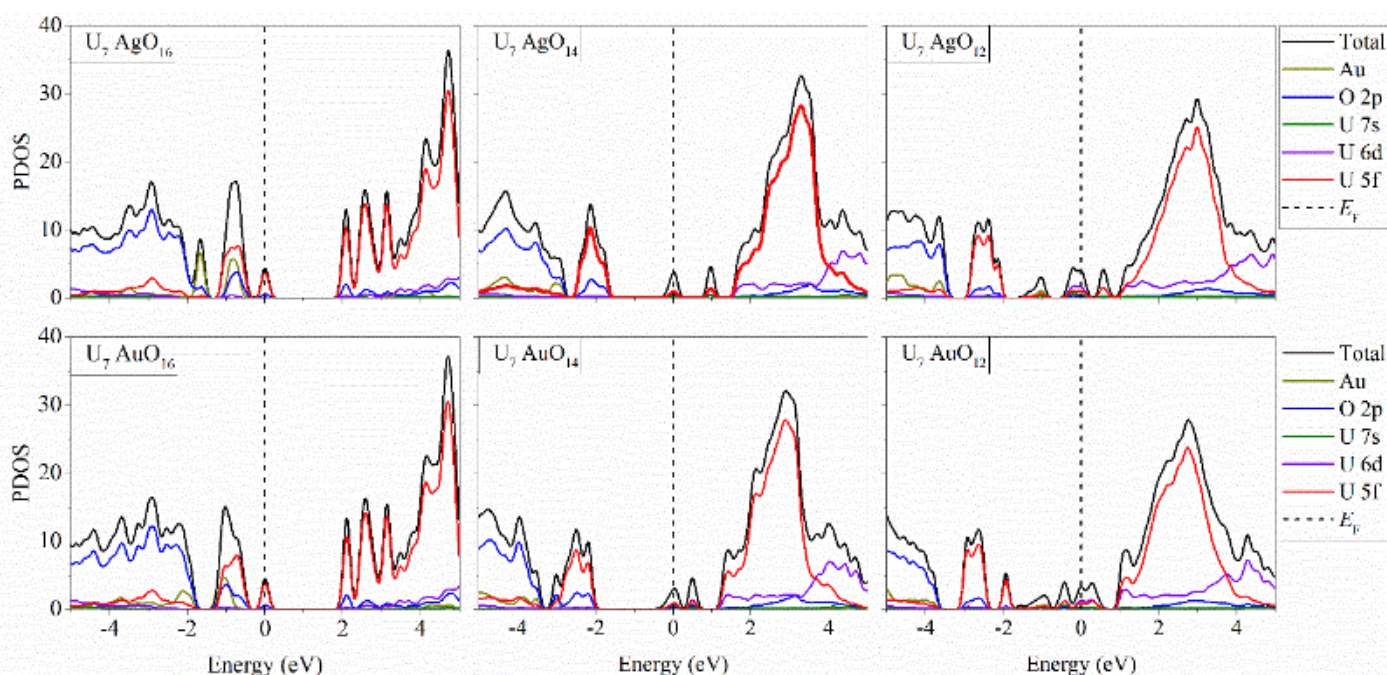
Figure 8 Partial spectra of electronic states obtained for uranium and oxygen with silver and gold [21].
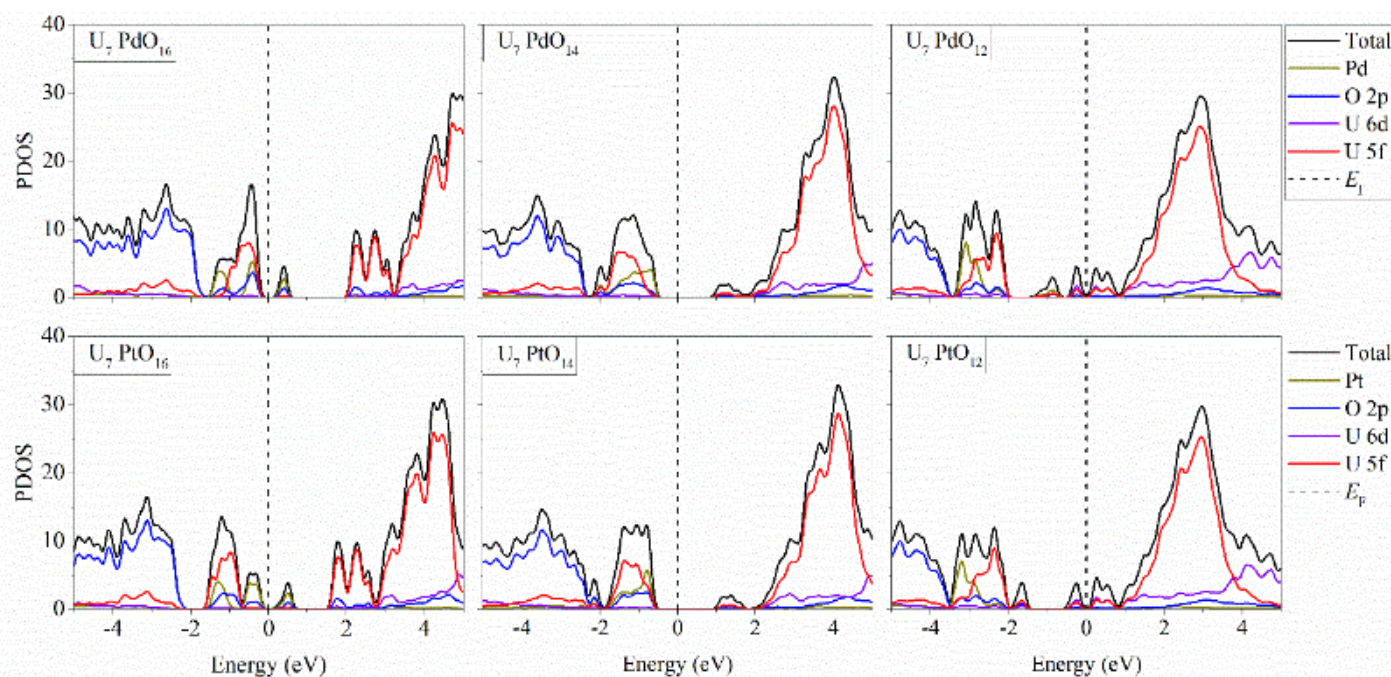
Figure 9 Partial spectra of electronic states obtained for compounds of uranium and oxygen with palladium and platinum [21].

Figure 10 Recognizing the bonding situations in U_7AgO_x by the COHP method [30]. The zero energy value, corresponding to the Fermi level, is shown by the horizontal dashed line.

However, doping with not all noble metals can cause electronic conductivity in uranium oxides. Similarly to those discussed above, the replacement of a U atom with a Pd or Pt atom in uranium oxides allows one only to vary the band gap of the semiconductor without leading to metallic conductivity (Figure 9). Moreover, the greatest narrowing of the band gap is observed for the compounds U_7PdO_{12} and U_7PtO_{12}, which is expressed in the values of its width: 0.044 and 0.028 eV, respectively.

In the case of a 1 : 15 ratio between the amount of noble metal and uranium in the oxide compound, the partial spectrum of the electron states indicates the presence of conductivity in the studied systems [30]. Conductivity in uranium oxides with an admixture of noble metals (Ag, Au, Pd, Pt) occurs due to the interaction of $2p$ electrons of oxygen with $5f$ electrons of uranium. Figure 10 shows the results of the bond analysis performed using the crystal orbital Hamilton population (COHP)

method for uranium oxides containing Ag. The method allows separating the energies of the band structure, leading to the densities of states. In other words, the matrix equation for the density of states is weighted by the elements of the Hamiltonian matrix [44]. Bonding and antibonding interactions are represented in Figure 10 by negative and positive COHP values, respectively. Zero COHP values indicate no binding in the interactions. The analysis for systems containing palladium, platinum and gold gives a result close to that given for the U_7AgO_x systems. The bonding and antibonding peaks correspond to the peaks obtained in the partial spectrum of the electronic states of the U_7AgO_x systems. For the U_7AgO_{12} system, the emerging bonding between silver electrons and uranium electrons, which exists in the valence band, is discovered. This atypical bonding leads to the convergence of Ag atom with the uranium atom. At certain oxygen concentrations, the same bonds appear between uranium and other noble metals (Au, Pt and Pd). In all of these cases, the noble metal (Me) atoms turn out to be negatively charged. A U-Me bond can be formed by reducing oxygen atoms in these oxide systems [30].

The small size of the system did not allow the authors of [21, 30] to create a lower concentration of noble metals in UO_2, which would better correspond to reality. Nevertheless, this information is useful and consistent. According to work [45], being in a solid dielectric medium (in this case, SNF), Ag atoms form clusters and are capable of creating an effect based on the migration of metallic inclusions controlled by an electric field. The recovered SNF may also contain lithium clusters, found as a suspension in the LiCl melt [46]. In an electric field, closely spaced Ag and Li clusters create a bipolar electrode, i.e. an electrode that is not mechanically connected to the power supply but has anode and cathode parts. Drifting Li^+ ions falling into the interval between such electrode clusters is displaced along the electric field. Li^+ ions, reaching the cluster cathode in a porous medium at high temperature, are reduced. Thus, chains of Li atoms are formed, which fill the pores and are detected after the reduction process is completed. This process occurs in a medium (tablet) with connected pores. The effect under consideration accelerates the chemical reduction process described by Equations (1) and (2).

Thus, the presence of noble metals in SNF makes it possible to accelerate the process of their electrochemical reduction. The results of work [21] can serve the development and improvement of technology for the electrochemical recovery of spent nuclear fuel. In the future, DFT studies of SNF recovery should be expanded. When modeling this process, it is important to study not only the physicochemical properties of the recovered

material, but also its microstructure. If porosity is insufficient and pore connectivity is reduced, difficulties may arise with the release of O^{2-} ions from spent fuel (UO_2) immersed in the cathode basket. This can lead to the cessation of the electrochemical reduction of UO_2 to U.

3.3. Study of the replacement of thorium with uranium and the adsorption of U atoms on the main surfaces of thorium

Thorium has no naturally occurring fissile isotopes. The breeding and combustion mode of thorium fuel is triggered by an external source of initiating neutrons, which initially generates ^{233}U from thorium. The initial neutron multiplication is created by either a spallation source, in an accelerator-driven system (ADS), or a fusion source, in a fusion-fission hybrid system (FFH). Moreover, FFH, as a rule, has an advantage over ADS with respect to energy production. This is due to the fact that the fusion driver can be energy self-sufficient. It sends electricity from the fission blanket entirely to the grid. In turn, accelerator drivers will always require some fraction of the electricity generated by the fission blanket. In other words, ADS constantly requires received energy to be used for internal power consumption. The thorium-uranium fuel cycle can be reproduced in fast breeder reactors. Further development is required to make the Th-U cycle practical. Along with the scanning tunneling microscope (STM) method, the DFT + U method can be used to investigate the surface properties of thorium oxide [47].

Figure 11 shows examples of doped $Th_{32-x}U_xO_{64}$ systems obtained after relaxation [26]. As can be seen in the figure, only a slight distortion of the cell geometry is observed when Th atoms are replaced by U atoms. The U^{4+} cation is smaller in size than the Th^{4+} cation by 0.005 nm. The introduction of smaller uranium cations into the lattice instead of thorium cations creates stress in the lattice. Calculation of the density of state (DOS) spectrum of pure ThO_2 revealed the band gap (4.36 eV) [48] of this insulator, which turned out to be significantly less than the experimental value (6–7 eV) [49]. The main charge carriers in the conduction band are Th $5f$ electrons, while O $2p$ states dominate in the valence band. The changes in the DOS spectrum caused by the introduction of U atoms are not associated with a change in the band gap but indicate a weakening of the cationic interaction compared to that of the pure compound.

The change in Barder charges for doped systems with an increase in dopant atoms from 1 to 7 is shown in Figure 12 [26]. Already the first doping leads to a decrease in the charge on Th atoms. With subsequent doping,
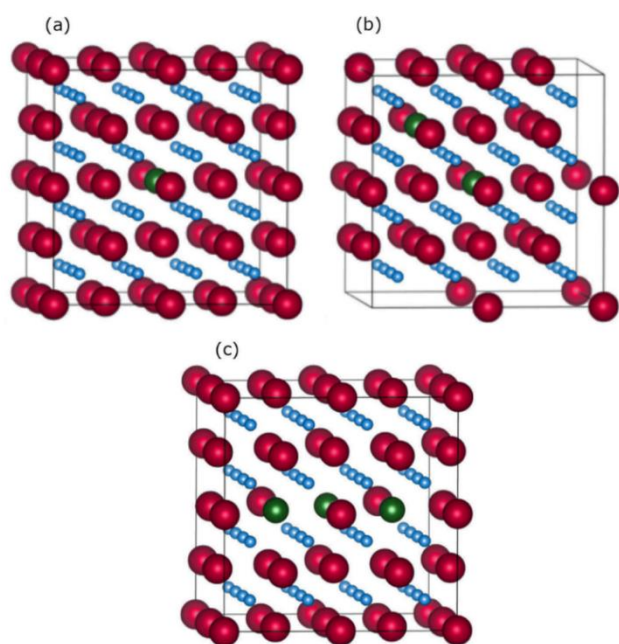
Figure 11 $Th_{32-x}U_xO_{64}$ supercells containing **(a)** one, **(b)** two, and **(c)** three uranium atoms after geometric optimization. Thorium, uranium, and oxygen atoms are represented in red, green, and blue, respectively [26].
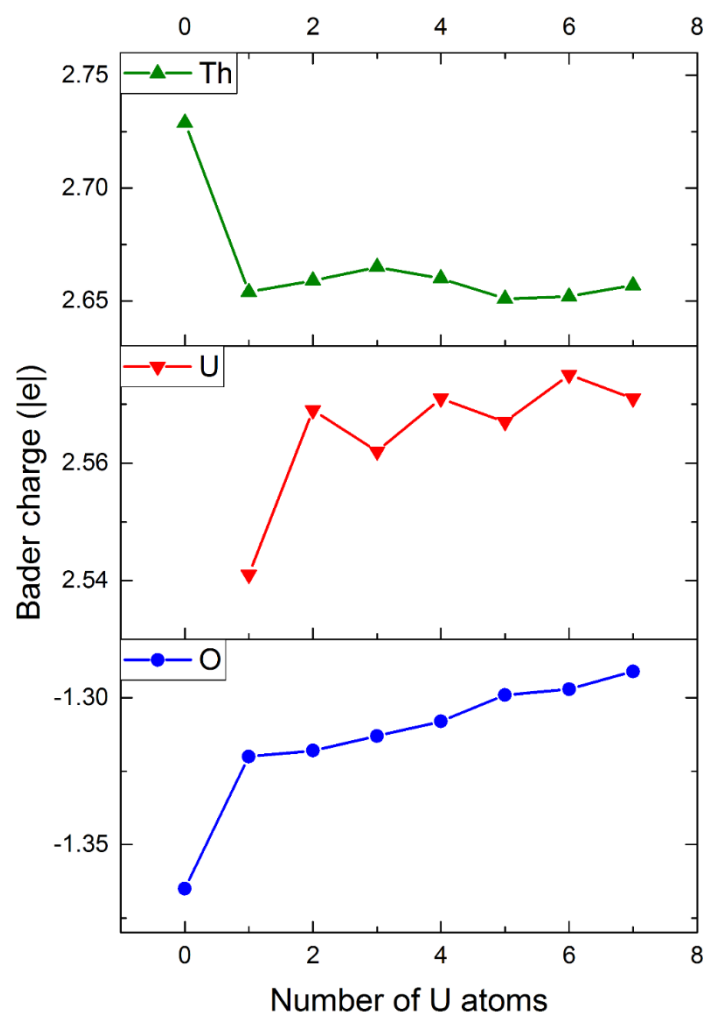
Figure 12 Average charges on the Th, U, and O ions in $Th_{(8-x)}U_xO_{16}$ [26].

the charge on Th atoms changes slightly and in a wave-like manner. At the same time, the charge on U atoms increases nonmonotonically as their number in the system increases. Simultaneously, after the introduction of the first U atom, an almost monotonic decrease in the absolute value of the charge on the O atoms occurs. Thus, the total charge of the system is maintained at approximately the same level, and this occurs mainly due to the redistribution of charges between the U and O atoms. This means that doping with uranium weakens the bonds between the Th and O atoms, i.e. makes thorium oxide fuel more capable of reduction.

The ThO₂ particles studied were confined to three surfaces: (100), (110) and (111). The (111) face has the lowest energy among them. The preferred site for the deposition of the U atom is the (100) surface, which has the lowest adsorption energy (–4.17 eV). The adsorption energy of the U atom on the (110) and (111) surfaces is –4.05 and –1.89 eV, respectively.

The calculated adsorption energies indicate that U adatoms will be adsorbed on all three surfaces, with particularly strong adsorption on the (100) and (110) surfaces. At the same time, the Wulff morphology for a ThO₂ particle equilibrium is a particle completely limited to the (111) surface orientation. Since the thorium fuel cycle has not yet been fully developed, the possibilities and challenges of using thorium in the nuclear fuel cycle are still being studied. There is now a need to properly assess the potential role of thorium in nuclear power in both the short and long term. To implement thorium fuel cycles, a variety of options must be considered, potential drivers explored, and ways to overcome current obstacles needed.

3.4. Thermophysical and mechanical properties of actinide dioxides

The development of fuels for nuclear reactors based on uranium, thorium, or plutonium, as well as the search for effective methods of reprocessing spent fuel, required fundamental data on the thermophysical properties of actinide oxides. In addition, understanding the consequences of the accumulation of fission products in fuel, a significant part of which belongs to the lanthanide group, has also become an urgent task [50]. Due to the complexity associated with the radioactivity of actinides, most of the new results have been obtained using computational methods such as molecular dynamics, DFT, or CALculation of PHAse Diagrams (CALPHAD) [51].

The isochoric heat capacity of UO₂ was calculated from the density of phonon states using the LDA + U DFT approach [52]. The heat capacity can be expressed as:

$$C_V = \sum_q k_B \left[\frac{\hbar\omega_q(V)}{2k_BT}\right]^2 cosh^2 \left[\frac{\hbar\omega_q(V)}{k_BT}\right]^2, \qquad \textbf{(6)}$$

where k_B is the Boltzmann constant, $\hbar$ is the reduced Planck constant and $\omega_q(V)$ is the frequency of the phonon with the wave vector q at constant volume V [53].

The $C_V(T)$ calculated dependence is compared with the experiment of Sanati et al. [54] in Figure 13. The heat capacity C_v of UO_2 with fluorite structure is in good agreement with experimental data up to room temperature. A significant deviation from the experimental dependence at higher temperatures is associated with the manifestation of anharmonicity.

Early actinides have a wider range of oxidation states and a more covalent type of interatomic bonds. Plutonium is the element from which the type of bonds becomes more ionic, and the range of oxidation states noticeably decreases. In addition, the ground states for UO_2 and NpO_2 are antiferromagnetic (AFM) [55, 56], while for PuO_2 the ground state is assumed to be either non-magnetic (NM) [57] or AFM [56].

Thermal conductivity is an important parameter for new technologies for SNF reprocessing. Increasing the thermal conductivity of a material promotes faster heat dissipation, which helps to avoid significant overheating and quickly regulate the temperature regime. The current understanding of lattice thermal conductivity at the atomic level remains incomplete. It is based on kinetic theory and relies on unit cell data.

Based on the data on the group velocity v_λ^α and the phonon distribution function F_λ^β, the lattice conductivity $\kappa_l^{\alpha\beta}$ of the crystal can be represented by the expression [58]:

$$\kappa_l^{\alpha\beta} = \frac{1}{k_BT^2\Omega N}\sum_\lambda f_0 (f_0+1)(\hbar\omega_\lambda)^2 v_\lambda^\alpha F_\lambda^\beta, \qquad \textbf{(7)}$$

where k_B, T, Ω, N and f_0 are the Boltzmann constant, temperature, unit cell volume, q-point grid, and the Bose-Einstein statistics, respectively.

By calculating the interatomic force constants by the DFT + U method and solving the Boltzmann transport equation for phonons, the lattice contribution to the thermal conductivity of UO_2 was determined [59]. Since UO_2 has a very low electrical conductivity, the electronic contribution to $\kappa_l^{\alpha\beta}$ was not taken into account. The $\kappa_l^{\alpha\beta}$ values for UO_2 differ greatly at high and low temperatures. So, at T = 3000 K $\kappa_l^{\alpha\beta}$ ~ 0.96 W · m⁻¹ · K⁻¹, and at T = 100 K $\kappa_l^{\alpha\beta}$ ~ 34 W · m⁻¹ · K⁻¹ (Figure 14). The calculated [59] and experimental [60] values of $\kappa_l^{\alpha\beta}$ are in
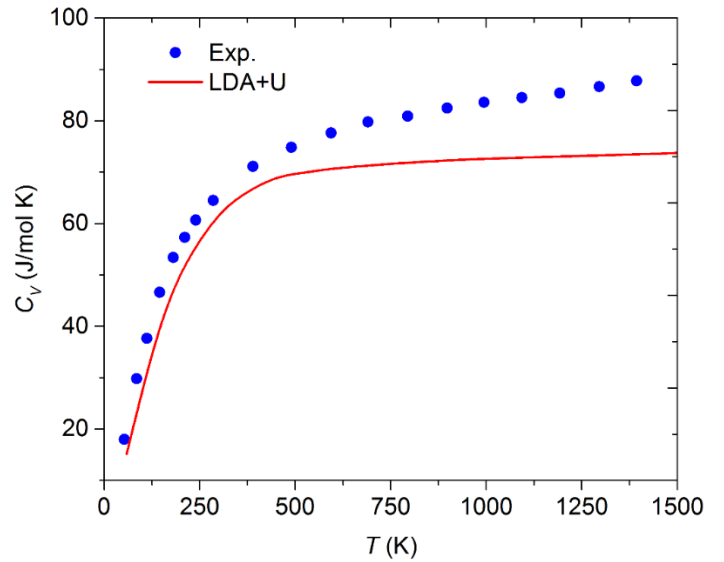
Figure 13 Temperature dependence of the isochoric heat capacity of UO_2, obtained experimentally [40] and calculated using the LDA + U approximation [52].
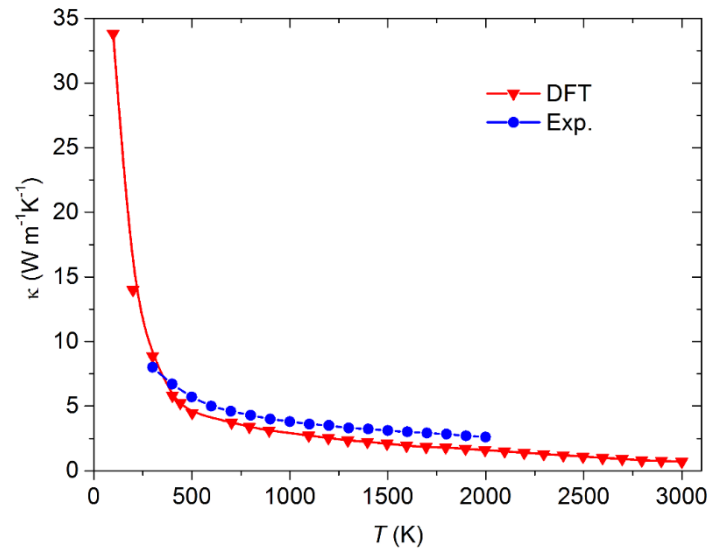
Figure 14 Temperature dependence of the lattice thermal conductivity of UO_2, determined using DFT + U calculations [58], along with the experimentally obtained value of the thermal conductivity [60].

good agreement. The lower calculated $\kappa_l^{\alpha\beta}$ values are explained by low group velocity, strong anharmonicity and phonon–phonon coupling of acoustic and low-frequency optical branches [59]. The latter circumstance leads to larger scattering, smaller mean free path, and shorter lifetime of phonons. However, the correct temperature $\kappa_l^{\alpha\beta}$ trend indicates that DFT + U calculations can play an important role in developing concepts of nuclear fuel thermal properties.

The mechanical properties of nuclear fuel are determined by many related mechanisms occurring at different scales. The temperature dependence of the bulk

modulus $B = -\frac{1}{V}\frac{\partial V}{\partial P}$ for PuO$_2$, obtained using DFT calculation in the framework of GGA and quasi-harmonic approximation is shown in Figure 15 [61]. We have not found experimental data for the temperature dependence of B of plutonium dioxide. However, comparisons can be made between the B values calculated at room temperature for PuO$_2$ (266 GPa), NpO$_2$ (200 GPa), UO$_2$ (211 GPa), and ThO$_2$ (198 GPa) [62].

In [63], a model of MOX fuel was constructed by laying layers of UO$_2$ and PuO$_2$ along the same tetragonal axis. At the same time, in the LDA + U model, different relationships between these components were used, and spin-orbit coupling was neglected. Elastic moduli, which are proportionality coefficients between stresses and their corresponding deformations, were calculated. They are specified using the generalized Hooke's law:

$$\sigma_{ij} = C_{ijkl}\varepsilon_{kl}, \qquad (8)$$

where σ_{ij} is the stress arising in the system deformed by the ε_{kl} value. The elastic moduli are reduced to a matrix symmetrical with respect to the main diagonal. The conditions of mechanical stability are expressed through the elastic moduli of the crystal. In particular, for a crystal with a tetragonal structure, these conditions are [64]:

$$C_{11} > 0; \;\; C_{33} > 0; \;\; C_{44} > 0; \;\; C_{66} > 0;$$
$$C_{11} - C_{12} > 0; \;\; C_{11} + C_{33} - 2C_{13} > 0; \qquad (9)$$
$$2(C_{11} + C_{12}) + C_{33} + 4C_{13} > 0.$$

All stability criteria for the crystalline oxide mixture Pu$_x$U$_{1-x}$O$_2$ calculated in the LDA + U model at various values of Pu concentration are presented in Figure 16 [63]. The condition for each criterion to be positive is met. Consequently, all mixed crystals with a tetragonal structure considered are stable at a temperature of 0 K. Bulk moduli can be expressed in terms of elastic moduli corresponding to a given crystal symmetry. It turned out that the calculated bulk modulus for PuO$_2$ based on the tetragonal lattice is close (within 1 GPa) to the above presented DFT + GGA results based on the fluorite lattice.

Currently, quantum chemical calculation methods are the main source of physicochemical data for the main actinide oxides. The data obtained by these methods are reliable enough to predict trends among different actinides. A detailed study of thermophysical properties will make it possible to predict the transition of the fuel to a higher burn-up, as well as a more efficient use of the

fissile composition of the fuel. Optimization based on these studies will lead to increased power generation and the corresponding economic benefits.
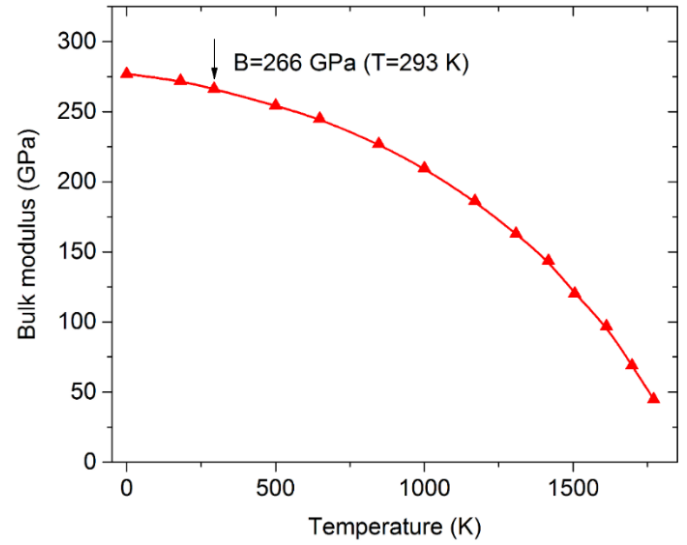
Figure 15 Temperature dependence of the bulk modulus of PuO$_2$ obtained using DFT calculations [61].
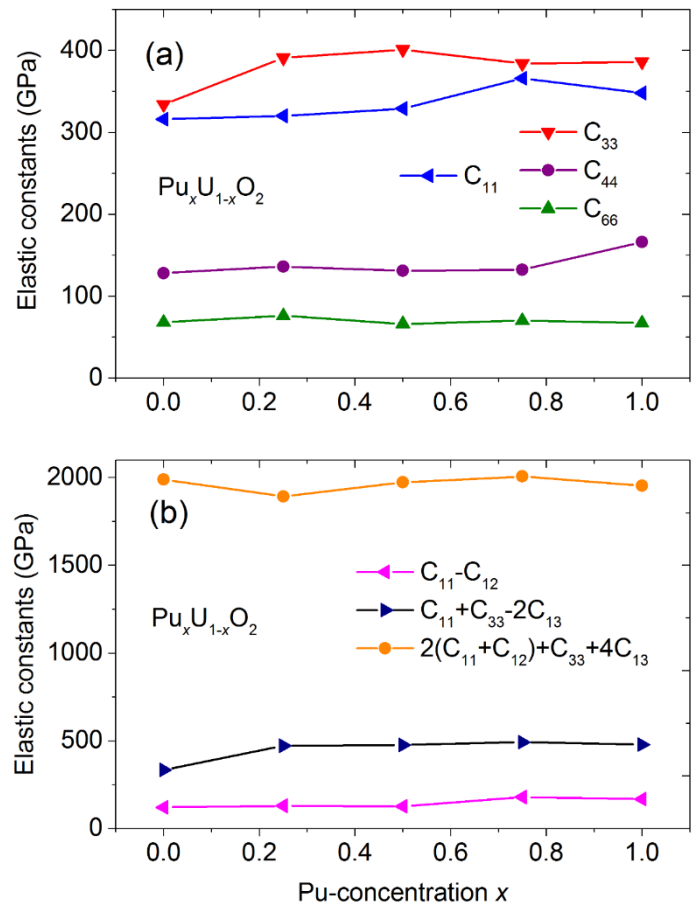
Figure 16 Calculated (a) elastic constants and (b) those combinations in units of GPa, for the Pu$_x$U$_{1-x}$O$_2$ compounds [63].

3.5. Lattice parameter, structural phase transition and melting temperatures of $Pu_xU_{1-x}O_2$ and U_xO_y compounds

According to Vegard's law, the lattice parameter depends linearly on the concentration of one component [65]. The lattice parameter a_0 calculated in [63] for the FM and AFM states of the $Pu_xU_{1-x}O_2$ compounds obeys Vegard's law with good accuracy (Figure 17a). It can also be noted that the lattice constant for all ordered compounds under consideration is always greater in AFM states, represented by a structure with layer-by-layer alternation of UO_2 and PuO_2 compounds, than in the ferromagnetic state (FM). The AFM* bicollinear structure for $Pu_{0.5}U_{0.5}O_2$, built by alternating UO_2 and PuO_2 layers, when two adjacent uranium layers are interrupted by two adjacent plutonium layers, is energetically unfavorable. In addition, the lattice constant for this structure has a very low value, falling outside the dependence of the AFM state. The results show that the energies of AFM states have lower values than the energies of FM states (Figure 17b). Thus, direct and reverse transitions between the FM and AFM states of both UO_2 and PuO_2 require a change in the crystal lattice parameter.

There is reason to believe that radioactive decay of U occurs in the deep mantle of the Earth. This decay is one of the main sources of heat on the Planet [66]. It has been experimentally shown that at high temperatures UO_2 has a fluorite-type structure up to pressures of ~ 18 GPa [67]. However, in the pressure range from 33 to 82 GPa it acquires orthorhombic structure.

Experiments using diamond anvil cells have shown that the transition from the cubic structure of UO_2 and ThO_2 to the orthorhombic structure occurs slowly and continues with increasing pressure [68]. For uranium dioxide, the initial value of the transition pressure is determined to be 42 GPa. However, the cubic phase of UO_2 was still present even at 69 GPa.

DFT calculations obtained by the GGA + U method showed that the pressure for the structural transition between stable phases of UO_2 (fluorite and cotunnite (orthorhombic structure)) was 20.6 GPa [69]. It was found that the Hubbard corrections (U_H and J_H) depend on the type of crystal structure. For cubic and orthorhombic structures, a correction U_H of 4.5 eV and 6.0 eV was used, respectively. Although the J_H correction (= 0.51 eV) was unchanged for both structures. Modeling of the structural phase transition in UO_2 using the VASP software package and the PAW was performed in [70]. The Hubbard parameters used to take into account the localization effect of the $5f$ orbital were identical to the data in [69].

The structural phase transition in this work was studied by creating hydrostatic pressure in a cell of constant shape. In Figure 18 the dependences of energy on the volume of the system $E(V)$ and the enthalpy difference as a function of pressure $\Delta H(P)$ are shown. The value of ΔH was determined as the difference between the enthalpies of the orthorhombic and cubic phases obtained under the same thermodynamic parameters. The found pressure at which the phase transition from the fluorite structure to the orthorhombic structure occurred is 46.8 GPa, which is in satisfactory agreement with the data of [68].

When studying the behavior of the cubic and orthorhombic phases of UO_2 over the entire range of positive pressures under consideration, it was found that the equilibrium collapse in volume is 6.4 % [70]. This is somewhat less than the similar characteristic (7.3 %) established in [71]. However, the change in volume for these phases at the phase transition pressure turned out to be ~ 5.3 % (Figure 19) [70]. Thus, the structural phase transition between the cubic and orthorhombic phases of UO_2 that occurs at high pressure is a first-order transition with a rather significant change in volume.
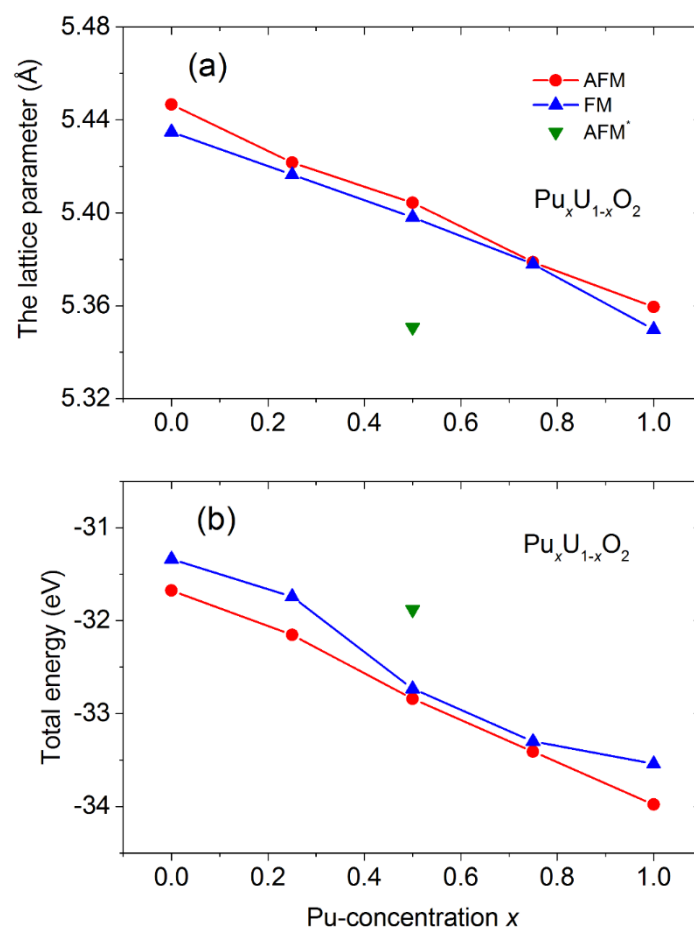
Figure 17 (a) the lattice parameter and (b) the total energy for different $Pu_xU_{1-x}O_2$ compound [63].
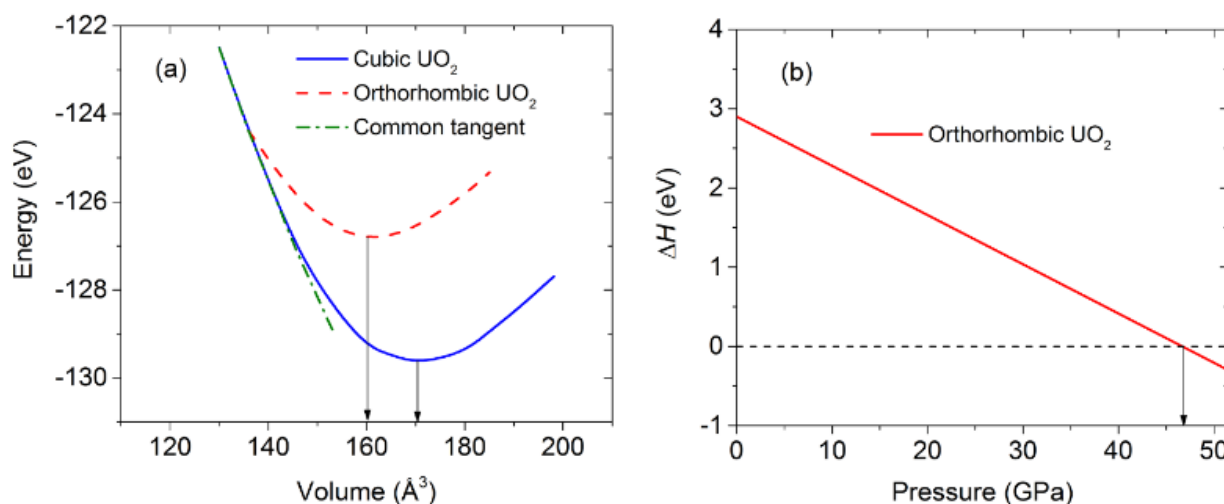
Figure 18 The variation of energy with respect to volume for UO_2. Here, volume at 0 GPa has been shown with arrows, and the common tangent has been shown by the dash-dotted line; (b) the variation of enthalpy differences with respect to pressure for UO_2, the arrow indicates phase transition pressure [70].
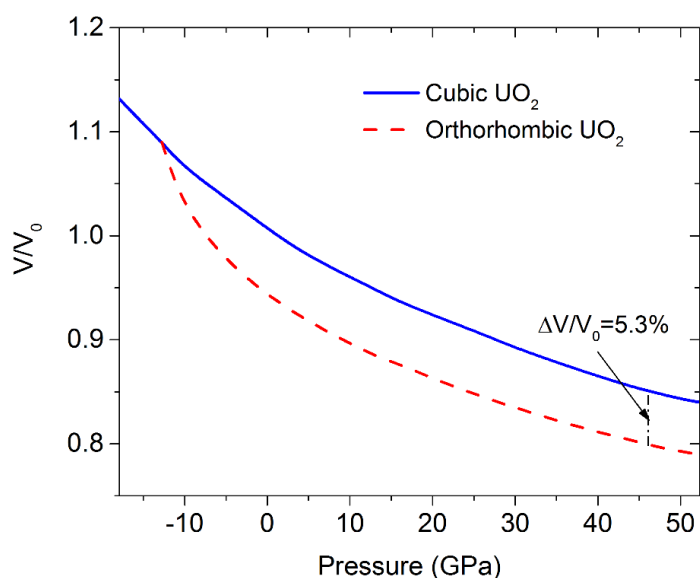
Figure 19 Dependence of relative volume on pressure obtained by compression of cubic and orthorhombic phases of UO_2; the arrow indicates the relative change in volume during a structural phase transition [70].

The data obtained above, related to the structural phase transition in UO_2, cannot be fully applied in practice because they refer to the temperature of absolute zero. For example, it is quite difficult to use them to characterize the processes occurring in the fuel element of a nuclear reactor. Indeed, at linear power generation levels 590 W/cm axial temperature in fuel element of the Pressurized Water Reactor (PWR) is 2550 K while the melting point of the ceramic UO_2 fuel is approximately 3130 K [72].

When combined with oxygen, uranium exhibits valences U^{4+}, U^{5+}, and U^{6+}. So, the lowest valence is in the compound UO_2, and the highest valence is in UO_3. Using the VASP software package based on ab initio quantum molecular dynamics simulations, melting temperatures for six stable uranium oxides were obtained, which are presented in Table 1 along with the corresponding melting densities [20].

These data provide guidance for future experiments, since experimental melting densities for most uranium oxides are not available in the literature. The calculated melting temperature for the four oxides U_4O_9, U_3O_7, U_2O_5, and U_3O_8 can be given as 2465 ± 65 K. The experimental melting temperatures of UO_2, NpO_2, PuO_2, and AmO_2 are 3140, 3070, 2663, and 2448 K, respectively [73].

The wave function of the $5f$ shell characteristic of actinides extends far from the core. As a consequence, $5f$ electrons can either adopt band states or exhibit localized behavior. This uncertainty in the status of $5f$ electrons leads to instability of the actinide crystal lattice. In particular, plutonium, when heated to its melting point,

Table 1 – The ambient melting points of the six uranium oxides, along with the corresponding melting densities ρ_m obtained from the ab initio method implemented with VASP [20].

Oxide	UO_2	U_4O_9	U_3O_7	U_2O_5	U_3O_8	UO_3
ρ_m, g/cm³	9.685	10.2	10.3	7.57	7.55	5.81
T_m, (K)	3100	2490	2530	2460	2380	1790

forms six allotropic forms. Experimental data on the thermodynamic properties of single crystals of actinide oxides are extremely scarce and subject to large uncertainties. This is due to the fact that growing such single crystals is difficult. An additional layer of complexity to this comes from the preparation and handling of radioactive material. For example, working with reactive, radioactive and toxic elements requires them to be sealed during crystal growth (usually in a quartz tube). The melting point and thermal conductivity determine the safety margins and behavior of the fuel in the reactor. Therefore, they are considered key parameters. The oxygen stoichiometry of the fuel significantly affects these properties. In this regard, the prediction of possible changes in the composition and its effect on thermophysical properties is of decisive importance.

4. Acceptable accuracy and increased speed of DFT calculations for actinide oxides

The result of the study [74] was the confirmation of experimental and theoretical data that the ground states for UO_2 and PuO_2 are AFM and NM, respectively. The best U_{eff} value for fitting the lattice parameter, magnetic moment and band gap in the case of UO_2 is 4.0 eV, and the recommended values for PuO_2 are defined as 4.0 eV and 4.5 eV. However, if the adjustment is made using the bandgap value, then $U_{eff} = 10$ eV should be taken for PuO_2.

In [75] a DFT study of the $U_{0.92}An_{0.08}O_2$ MOX surfaces (An = Np, Pu, Am and Cm) {1 1 1}, {1 1 0} and {1 0 0} was conducted. Various positions of An substitution (surface or subsurface) and increasing the ratio of An to U are considered. Substitution of U atoms by An lengthens the surface An-O bonds and shortens the U-O bonds. The elongation of An-O bonds stops as the An to U ratio increases.

The synthesized PuO_2 and NpO_2 films were studied using both X-ray absorption near edge structure (XANES) and extended X-ray absorption fine structure (EXAFS) measurements [76]. Calculation of DOS for actinide dioxides (NpO_2, PuO_2, AmO_2, and CmO_2) was carried out for various values of U_{eff} corrections with a step of 1 eV [77]. In Figure 20, as an example, the change in the band gap of NpO_2 depending on the value of U_{eff} is shown. The band gap continuously increases with increasing U_{eff} and reaches experimental values (2.85 ± 0.1 eV) in the vicinity of $U_{eff} = 4.5$–5.0 eV. Similar calculations for AmO_2 show that the correct value U_{eff} should be 4 eV. The lack of experimental data on the band gap for CmO_2

did not allow us to determine the value of the U_{eff} correction for this oxide.

Despite the fact that the values of U_{eff} are often selected empirically, this quantity has a precise physical meaning and can be determined in several ways. The linear response approach is based on the calculation of the second derivative of the total energy of the ground state with respect to the occupation number, which is considered as the Hubbard correction [78]. The correction U_{eff} established in this way has a strong dependence on the distance between the nearest neighbors and on the chemical element. The corrections U_{eff} calculated by this method for uranium and plutonium have a significantly lower value (more than 2 times) [79] than the corresponding corrections used to reproduce adequately the width of the band gap [26]. Calculations of the U_{eff} correction using constrained random-phase approximation (cRPA) [80], [81] or constrained density-functional theory (DFT) [82], [83] give highly divergent results themselves. The frequency-dependent U_{eff} in the random phase model inevitably depends on the choice of the one-particle basis. The calculations use only one of many possible sets of single-particle orbitals. The decrease in U_{eff} values in DFT calculations may be due to the lack of consideration of the relaxation of other (non-transition) orbitals. In addition, the shielding effect should be included more correctly in the calculation of U_{eff}.

DFT calculations are only part of ab initio methods. These methods are used to solve the electronic Schrödinger equation in order to yield the necessary quantum chemistry parameters. Earlier ab initio calculations were used to study the distinctive features of
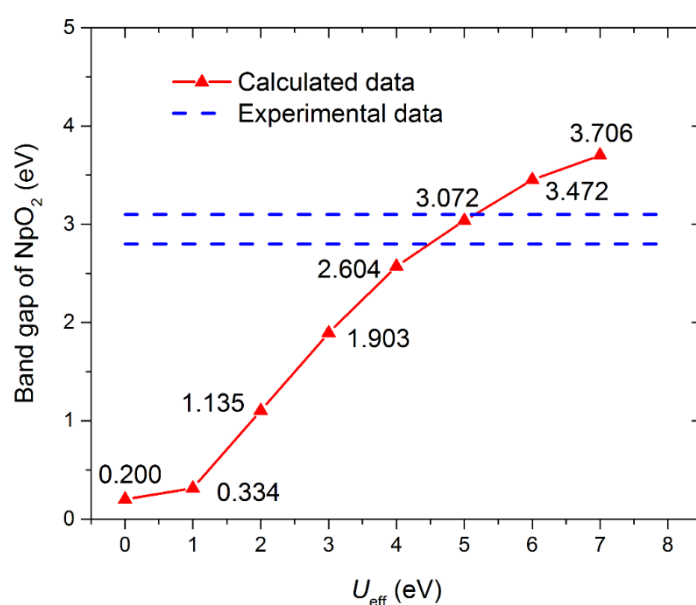

Figure 20 The band gap of NpO_2 [77].

actinide isotopes, as well as to study the nature of binding in "bare" molecules and clusters containing actinides [84]. The first-principles methods that do not use the DFT approximation are the DCHF method [85], where the four-component Dirac-Coulomb Hamiltonian (DC) is used together with the Hartree-Fock wave function (HF), and the Moller-Plesset second-order perturbation theory (MP2) [86, 87]. The same type of methods includes three different relativistic methods (all-electron scalar four component Dyall RESC method (AE), relativistic small-core ECPs, and zeroth order regular approximation ZORA) and several other methods [84, 88].

However, the most common method for first-principles study of the physicochemical properties of actinide oxides is DFT calculations using a periodic model within the framework of the GGA [89, 90]. An alternative to these calculations is calculations using configuration wave functions that also take into account the spin-orbit interaction. In [91], a detailed study of the geometry, electronic structure and vibration frequencies of two isoelectronic compounds PuO_2^{2+} and PuN_2 was carried out using both DFT and multi-configurational ab initio levels of theory, taking into account spin-orbital interaction. Moreover, in the latter case, dynamic correlation was taken into account using second-order perturbation theory and the variational difference-dedicated configuration interaction method. A comparison of these methods shows that DFTs provide a reasonable description of the electronic properties of the ground states of the open-shell systems under consideration. The consequence of this is a completely good description of the structural and vibrational properties. DFT calculations using the GGA approximation are also more successful than hybrid versions in calculating rotational properties. Spin-orbit effects have a weak effect on the geometry and vibrational frequencies in the ground states, but completely transform the distribution of electronic excited states.

In [92], a systematic study of the structural, electronic and magnetic properties of actinide oxides, nitrides and carbides (An_xX_y, An = U, Pu, Np; X = O, N, C) was carried out using the Heyd-Scuseria-Ernzerhof (HSE) hybrid functional, as well as the DFT method in the PBE and PBE + U approximation. HSE calculations for actinide oxides showed good agreement with experiments on the structural, electronic and magnetic properties. However, in the case of nitrides and carbides, this approximation does not produce sufficiently correct results. At the same time, the density of states calculated for nitrides and carbides can be better described using DFT calculations and the PBE approximation.

When experimental work is supplemented with computational methods, the true causes of the occurring processes can be identified, and their deep understanding can be ensured. The value of DFT calculations increases greatly as the size of the system increases. However, performing DFT calculations with a large number of atoms is unlikely because the computational effort required for these calculations increases rapidly as the size of the system increases. The time spent on the "standard" simulation is $t \sim N^3$, where N is the number of particles in the system. The development of so-called linear scaling methods, where $t \sim N$, will allow us to overcome this difficulty to a certain extent [93]. The transition to an algorithm with linear scaling DFT calculations is possible if we abandon the concept of extended Kohn-Sham orbitals, using other quantities that are strictly localized [94]. However, for now, linear scaling methods begin to work when the system contains on the order of several hundred atoms. In addition, the implementation of the DFT algorithm with linear scaling often introduces some, usually small errors.

5. Conclusions

DFT calculations have shown the ability of uranium to form short, strong bonds with oxygen and with a deficiency of oxygen in UO_2 and the presence of noble metals in it to create bonds with these metals. To date, computational chemistry of actinide oxides has not yet reached the necessary level where calculations performed using modern high-performance computing resources could effectively replace dangerous and difficult-to-perform physical experiments that provide new data on the properties of spent nuclear fuel. There are still no comprehensive data on the changes in the unit cell associated with corrosion and internal stresses, as well as the dissolution of metals in the oxide fuel. The corrosion effects observed in the uranium dioxide and zirconium alloys, from which the cladding is made, have not been studied, as well as the interaction of this system with boric acid, which is formed at Pressurized Water Reactor operations. Despite the difficulty in performing experiments on oxide nuclear fuels, it seems necessary to study oxidation reactions by cyclic voltammetry to obtain data on chemisorption and other types of reactions. More accurate data on oxygen diffusion in actinide oxides can be obtained by neutron diffraction. These and other physical experiments are a valuable method for guiding and determining the accuracy of DFT and ab initio molecular dynamics calculations. From the point of view of pyroreprocessing, the studies of the microkinetics of SNF dissolution in molten salt are of interest. For now, the main chemistry of reduction-oxidation is presented at the thermodynamic level. These data can also be used to guide numerical calculations. In connection with the upcoming

expansion of the use of fast reactors, a more detailed study of the properties of the α phase of metallic uranium and MOX fuel is of considerable interest. The use of more powerful computers and more complex algorithms will significantly expand the areas of research, providing a much more complete picture of the reactions occurring during the electrolytic reduction of SNF.

Supplementary materials

No supplementary materials are available.

Funding

Acknowledgments

Author contributions

Alexander Galashev: Writing – Review & Editing; Writing – Original draft; Visualization; Validation; Supervision; Software; Resources; Methodology; Investigation; Formal analysis; Data curation; Conceptualization.

Conflict of interest

The author declares that he has no known competing financial interests or personal relationships that could have appeared to influence the work reported in this paper.

Additional information

Scientific group website:

http://watercluster.ucoz.ru/

References

1. Ripani M, Energy from nuclear fission, Eur. Phys. J. Conf., **268** (2022) 00010. https://doi.org/10.1051/epjconf/202226800010

2. Galashev AY, Recovery of actinides and fission products from spent nuclear fuel via electrolytic reduction: Thematic overview, Int. J. Energy Res., **46(5)** (2021) 3891–3905. https://doi.org/10.1002/er.7458

3. Galashev AY, Processing of fast neutron reactor fuel by electrorefining: Thematic overview, Int. J. Energy Res., **45** (2020) 11459–11478. https://doi.org/10.1002/er.6267

4. Van Winckel S, Alvarez-Sarandes R, Purrov DS, Aldave de las Heras L, Assay data of spent nuclear fuel: the lab-work behind the numbers, Front. Energy Res., **11** (2023) 1168460. https://doi.org/10.3389/fenrg.2023.1168460

5. Pegg JT, Aparicio-Angles X, Storr M, de Leeuw NH, DFT+U study of the structures and properties of the actinide dioxides, J. Nucl. Mater., **492** (2017) 269–278. https://doi.org/10.1016/j.jnucmat.2017.05.025

6. Wang B-T, Shi H, Li W, Zhang P, First-principles LDA+U and GGA+U study of neptunium dioxide, Phys. Rev. B, **81** (2010) 045119. https://doi.org/10.1103/PhysRevB.81.045119

7. Moten SA, Atta-Fynn R, Ray AK, Muhammad N., Huda MN, Size effects on the electronic and magnetic properties of PuO_2 (111) surface, J. Nucl. Mater., **468** (2016) 37–45. https://doi.org/10.1016/j.jnucmat.2015.11.009

8. Gueneau C, Dupin N, Sundman B, Martial C, et al., Thermodynamic modelling of advanced oxide and carbide nuclear fuels: Description of the U–Pu–O–C systems, J. Nucl. Mater., **419** (2011) 145–167. https://doi.org/10.1016/j.jnucmat.2011.07.033

9. Dennett CA, Poudel N, Simmons PJ, Tiwari A, et al., Towards actinide heterostructure synthesis and science, Nature Commun., **13** (2022) 2221. https://doi.org/10.1038/s41467-022-29817-0

10. Suzuki M-T, Magnani N, Oppeneer PM, Microscopic theory of the insulating electronic ground states of the actinide dioxides AnO_2 (An = U, Np, Pu, Am, and Cm), Phys. Rev. B, **88** (2013) 195146. https://doi.org/10.1103/PhysRevB.88.195146

11. Shi H, Chu M, Zhang P, Optical properties of UO_2 and PuO_2, J. Nucl. Mater., **400(2)** (2010) 151–156. https://doi.org/10.1016/j.jnucmat.2010.02.024

12. Wang H, Konashi K, LDA + U study of Pu and PuO_2 on ground state with spin–orbital coupling, J. Alloys Compounds, **533** (2012) 53–57. https://doi.org/10.1016/j.jallcom.2012.03.117

13. Noutack MST, Geneste G, Jomard G, Freyss M, Investigation of the bulk and point defect properties in uranium–plutonium mixed oxides $(U,Pu)O_2$ using DFT+U: Effect of a low americium content, J. Appl. Phys., **131** (2022) 225106. https://doi.org/10.1063/5.0090000

14. Zhu J, Shi D, The electronic and mechanical properties of $(U, Th)O_2$ compounds: a first-principles study, RSC Adv., **13** (2023) 7206–7211. https://doi.org/10.1039/D3RA00018D

15. Dorado B, Garcia P, First-principles DFT + U modeling of actinide-based alloys: Application to paramagnetic phasesof UO_2 and (U,Pu) mixed oxides, Phys. Rev. B, **87** (2013) 195139. https://doi.org/10.1103/PhysRevB.87.195139

16. Burakovsky L, Ramsey SD, Baty RS, Ambient melting behavior of stoichiometric uranium-plutonium mixed oxide fuel, Appl. Sci., **13** (2023) 6303. https://doi.org/10.3390/app13106303

17. Fouquet-Métivier P, Martin PM, Manara D, Dardenne K, et al., Investigation of the solid/liquid phase transitions in the U–Pu–O system, Calphad, **80** (2023) 102523. https://doi.org/10.1016/j.calphad.2022.102523

18. Sheykhi S, Payami M, First-principles study of UO_2 lattice thermal-conductivity: A simple description, Iran J. Sci. Technol., **44(8)** (2020) 2585–1593. https://doi.org/10.1007/s40995-020-00927-y

19. Mir SH, Jha PC, Islam MS, Banerjee A, et al., Static and dynamical properties of heavy actinide monopnictides of

lutetium, Sci. Rep., **6** (2016) 29309. https://doi.org/10.1038/srep29309

20. Burakovsky L, Ramsey SD, Baty RS, Ambient melting behavior of stoichiometric uranium oxides, Front. Nucl. Eng., **2** (2024) 1215418. https://doi.org/10.3389/fnuen.2023.1215418

21. Vorob'ev AS, Galashev AY, Zaikov YuP, Quantum mechanical study of the influence of noble metals on the process of reduction of uranium oxides, Nucl. Eng. Technol., (2024). In press. https://doi.org/10.1016/j.net.2024.09.020

22. Galashev A, Abramova K, Vorob'ev A, Rakhmanova O, Zaikov Yu, Modeling the UO_2 reduction process, Electrochem. Mater. Technol., **2** (2023) 20232017. http://dx.doi.org/10.15826/elmattech.2023.2.017

23. Dudarev SL, Botton GA, Savrasov SY, Humphreys C, et al., Electron-energy-loss spectra and the structural stability of nickel oxide: An LSDA+U study, Phys. Rev. B, **57(3)** (1998) 1505–1509. https://doi.org/10.1103/PhysRevB.57.1505

24. Monkhorst HJ, Pack JD, Special points for Brillouin-zone integrations, Phys. Rev. B, **13(12)** (1976) 5188–5192. https://doi.org/10.1103/PhysRevB.13.5188

25. Perdew JP, Zunger A, Self-interaction correction to density-functional approximations for many-electron systems, Phys. Rev. B, **23(10)** (1981) 5048–5079. https://doi.org/10.1103/PhysRevB.23.5048

26. Shields AE, Santos-Carballal D, de Leeuw NH, A density functional theory study of uranium-doped thoria and uranium adatoms on the major surfaces of thorium dioxide, J. Nucl. Mater., **473** (2016) 99–111. https://doi.org/10.1016/j.jnucmat.2016.02.009

27. Perdew JP, Burke K, Ernzerhof M, Generalized gradient approximation made simple, Phys. Rev. Lett., **77** (1996) 3865–3868. https://doi.org/10.1103/PhysRevB.23.5048

28. Kresse G, Joubert D, From ultrasoft pseudopotentials to the projector augmented-wave method, Phys. Rev. B, **59** (1999) 1758–1775. http://dx.doi.org/10.1103/PhysRevB.59.1758

29. Blochl PE, Projector augmented-wave method, Phys. Rev. B, **50** (1994) 17953–17979. https://doi.org/10.1103/PhysRevB.50.17953

30. Galashev AY, Vorob'ev AS, Zaikov YuP, Quantum-mechanical study of the electronic properties of $U_xPu_yO_z$ compounds formed during the recovery of spent nuclear fuel, J. Serb. Chem. Soc., **88(11)** (2023) 1125–1134. https://doi.org/10.2298/JSC230213038G

31. Abdulaziz R, Brown L, Inman D, Sharrad CA, et al., Electrochemical reduction of UO_2 to U in LiCl-KCl molten salt eutectic using the fluidized cathode process, J. Electrochem. Soc., **164(8)** (2017) H5280. https://doi.org/10.1149/2.0421708jes

32. Jamal GEl, Gouder T, Eloirdi R, Jonsson M, Idriss H, Monitoring the reduction of UO_3 thin film by hydrogen atoms using valence-level spectroscopy: correlating the U5f[1] signal to surface hydroxyls, Front. Fuels, **1** (2023) 1303890. https://doi.org/10.3389/ffuel.2023.1303890

33. Shundalaua MB, Zajogina AP, Komiaka AI, SokolskyaAA, Umreiko DS, DFT modeling of the uranium trioxide vibration spectra characteristics, J. Spectrosc. Dyn., **2** (2012) 19. https://elib.bsu.by/bitstream/123456789/160888/2/110637239.pdf

34. Kaloni TP, Onder N, Pencer J, Torres E, DFT+U approach on the electronic and thermal properties of

hypostoichiometric UO_2, Ann. Nucl. Energy, **144** (2020) 107511. https://doi.org/10.1016/j.anucene.2020.107511

35. Dugan CL, Peterson GG, Mock A, Young C, et al., Electrical and material properties of hydrothermally grown single crystal (111) UO_2, Eur. Phys. J. B, **91** (2018) 67. https://doi.org/10.1140/epjb/e2018-80489-x

36. Choi E-Y, Kim J-K, Im H-S, Choi I-K, et al., Effect of the UO_2 form on the electrochemical reduction rate in a LiCl–Li_2O molten salt, J. Nucl. Mater., **437** (2013) 178–187. https://doi.org/10.1016/j.jnucmat.2013.01.306

37. Hur J-M, Hong S-S, Lee H, Electrochemical reduction of UO_2 to U in a LiCl–KCl–Li_2O molten salt, J. Radioanal. Nucl. Chem., **295** (2013) 851–854. https://doi.org/10.1007/s10967-012-2258-0

38. Choi E-Y, Won C-Y, Cha J-S, Park W, et al., Electrochemical reduction of UO_2 in LiCl–Li_2O molten salt using porous and nonporous anode shrouds, J. Nucl. Mater., **444** (2014) 261–269. https://doi.org/10.1016/j.jnucmat.2013.09.061

39. Choi E-Y, Jeong SM, Electrochemical processing of spent nuclear fuels: An overview of oxide reduction in pyroprocessing technology, Prog. Nat. Sci.: Mater. Intern., **25(6)** (2015) 572–582. https://doi.org/10.1016/j.pnsc.2015.11.001

40. Kim SW, Lee SK, Kang HW, Choi EY, et al., Electrochemical properties of noble metal anodes for electrolytic reduction of uranium oxide, J. Radioanal. Nucl. Chem., **311** (2017) 809–814. https://doi.org/10.1007/s10967-016-5107-8

41. Broczkowsk ME, Goldic JS, Noel J, Shoesmith DW, Influence of noble metal particles on redox reactions on uranium dioxide surfaces, Adv. Sci. Technol., **45** (2006) 1996–2003. https://doi.org/10.4028/www.scientific.net/AST.45.1996

42. Shishkin AV, Shishkin VYu, Pankratov AA, Burdina AA, Zaikov YuP, Electrochemical reduction of La_2O_3, Nd_2O_3, and CeO_2 in LiCl-Li_2O melt, Materials, **15(11)** (2022) 3963. https://doi.org/10.3390/ma15113963

43. Shishkin AV, Shishkin VYu, Maslennikova AA, Salyulev A, et al., Electrochemical reduction of Pd-Nd_2O_3-CeO_2 mixtures in the LiCl-Li_2O melt, Processes, **11(6)** (2023) 1599. https://doi.org/10.3390/pr11061599

44. Steinberg S, R. Dronskowski R, The crystal orbital Hamilton population (COHP) method as a tool to visualize and analyze chemical bonding in intermetallic compounds, Crystals, **8(5)** (2018) 225. https://doi.org/10.3390/cryst8050225

45. Yang Y, Gao P, Li L, Pan X, et al., Electrochemical dynamics of nanoscale metallic inclusions in dielectrics., Nat. Commun., **5** (2014) 4232. https://doi.org/10.1038/ncomms5232

46. Merwin A, Phillips WC, Williamson MA, Willit JL, et al., Presence of Li clusters in molten LiCl-Li, Sci. Rep., **6** (2016) 25435. https://doi.org/10.1038/srep25435

47. Szpunar B, Szpunar J, Thoria ehancement of nuclear reactor safety, Phys. Int., **4(2)** (2013) 110–119. https://doi.org/10.3844/pisp.2013.110.119

48. Liu B, Aidhy DS, Zhang Y, Weber WJ, Theoretical investigation of thermodynamicstability and mobility of the oxygen vacancyin ThO_2–UO_2 solid solutions, Phys. Chem. Chem. Phys., **16** (2014) 25461–25467. https://doi.org/10.1039/c4cp03660c

49. Kelly TD, Petrosky JC, Turner D, McClory JW, Mann JM, The unoccupied electronic structure characterization of hydrothermally grown ThO_2 single crystals, Phys. Status. Solidi RRL, **8(3)** (2014) 283–286. https://doi.org/10.1002/pssr.201308286

50. Konings RJM, Benes O, Kovacs A, Manara D, et al., The thermodynamic properties of the f-elements and their compounds. Part 2. The lanthanide and actinide oxides, J. Phys. Chem. Ref. Data, **43(1)** (2014) 013101. https://doi.org/10.1063/1.4825256

51. Korotaev P, Yanilkin AV, Steels classification by machine learning and calphad methods, Calphad, **82(5)** (2023) 102587. https://doi.org/10.1016/j.calphad.2023.102587

52. Wang B-T, Zhang P, Lizárraga R, Di Marco I, Eriksson O, Phonon spectrum, thermodynamic properties, and pressure-temperature phase diagram of uranium dioxide, Phys. Rev. B, **88** (2013) 104107. https://doi.org/10.1103/PhysRevB.88.104107

53. Wang R, Wang S, Wu X, Ab initio study of the thermodynamic properties of rare-earth-magnesium intermetallics MgRE (RE=Y, Dy, Pr, Tb), Physica Scripta, **83** (2011) 065707. https://doi.org/10.1088/0031-8949/83/06/065707

54. Sanati M, Albers R, Lookman T, Saxena A, Elastic constants, phonon density of states, and thermal properties of UO_2, Phys. Rev. B, **84** (2011) 014116. https://doi.org/10.1103/PhysRevB.84.014116

55. Sharma Y, Paudel B, Huon A, Schneider MM, et al., Induced ferromagnetism in epitaxial uranium dioxide thin films, Adv. Sci., **9(33)** (2022) 2203473. https://doi.org/10.1002/advs.202203473

56. Pegg JT, Shields AE, Storr MT, Wills AS, et al., Magnetic structure of UO_2 and NpO_2 by first-principle methods, Phys. Chem. Chem. Phys., **21** (2019) 760–771. https://doi.org/10.1039/C8CP03581D

57. Gao H, Li M, Yang Y, Zhang P, First-principles calculation of structural, magnetic and electronic properties of PuO_2-H , 0≤x≤2, J. Alloys Compounds, **857** (2020) 157592. https://doi.org/10.1016/j.jallcom.2020.157592

58. Islam M, DFT and DFT+U Insights into the physical properties of UO_2, J. Sci. Res., **15(3)** (2023) 739–757. http://doi.org/10.3329/jsr.v15i3.64394

59. Torres E, Kaloni TP, Thermal conductivity and diffusion mechanisms of noble gases in uranium dioxide: A DFT+U study, J. Nucl. Mater., **521** (2019) 37–45. https://doi.org/10.1016/j.jnucmat.2019.04.040

60. Fink JK, Thermophysical properties of uranium dioxide., J. Nucl. Mater., **279(1)** (2000) 1–18. https://doi.org/10.1016/S0022-3115(99)00273-1

61. Minamoto S, Kato M, Konashi K, Kawazoe Y, Calculations of thermodynamic properties of PuO_2 by the first-principles and lattice vibration, J. Nucl. Mater., **385(1)** (2009) 18–20. https://doi.org/10.1016/j.jnucmat.2008.10.024

62. Sobolev V, Modelling thermal properties of actinide dioxide fuels, J. Nucl. Mater., **344(1–3)** (2005) 198–205. https://doi.org/10.1016/j.jnucmat.2005.04.042

63. Yang Y, Wang B, Zhang P, Electronic and mechanical properties of ordered (Pu, U) O_2 compounds: A density functional theory +U study, J. Nucl. Mater., **433(1–3)** (2013) 345–350. https://doi.org/10.1016/j.jnucmat.2012.10.027

64. Nye JF. Physical properties of crystals. Oxford University Press: Oxford; 1985. 352 p. ISBN 9780198511656

65. Cognini L, Pizzocri D, Barani T, Van Uffelen P, et al., Helium solubility in oxide nuclear fuel: Derivation of new correlations for Henry's constant, Nucl. Eng. Design, **340** (2018) 240–244. https://doi.org/10.1016/j.jnucmat.2022.153777

66. Terez EI, Terez IE, Thermonuclear reaction as the main source of the Earth's energy, Int. J. Astron. Astrophys., **3** (2013) 362–365. http://dx.doi.org/10.4236/ijaa.2013.33040

67. Greaux S, Gautron L, Andrault D, Bolfan N, et al., Structural characterization of natural UO_2 at pressures up to 82 GPa and temperatures up to 2200 K, Am. Mineralogist, **93(7)** (2008) 1090–1098. http://dx.doi.org/10.2138/am.2008.2735

68. Idiri M, Le Bihan T, Heathman S, Rebizant J, Behavior of actinide dioxides under pressure: UO_2 and ThO_2, Phys. Rev. B, **70** (2004) 14113. https://doi.org/10.1103/PhysRevB.70.014113

69. Tian X, Wang Y, Ge L, Dong W, et al., First principles calculation of UO_2 polymorphs and phase transitions under compressive and tensile loading, Comput. Mater. Sci., **169** (2019) 109124. https://doi.org/10.1016/j.commatsci.2019.109124

70. Singh S, Sonvane Y, Nekrasov KA, Boyarchenkov AS, et al., Systematic investigation of electronic, mechanical and optical properties of UO_2 at higher pressure: A DFT+U+SOC study, Solid State Sci., **132** (2022) 106968. https://doi.org/10.1016/j.solidstatesciences.2022.106968

71. Yu J, Devanathan R, Weber WJ, First-principles study of defects and phase transition in UO_2, J. Phys. Condens. Mater., **21(43)** (2005) 435401. https://doi.org/10.1088/0953-8984/21/43/435401

72. Yadigaroglu G, Nuclear reactors: Physics and materials, CHIMIA Int. J. Chem., **59(12)** (2005) 877–886. https://doi.org/10.2533/000942905777675318

73. Chollet M, Prieur D, Böhler R, Belina R, Manara D, The melting behaviour of uranium/neptunium mixed oxides, J. Chem. Thermodynamics, **89** (2015) 27–34. http://dx.doi.org/10.1016/j.jct.2015.04.031

74. Chen J-L, Kaltsoyannis N, DFT + U study of uranium dioxide and plutonium dioxide with occupation matrix control, J. Phys. Chem. C, **126** (2022) 11426−11435. https://doi.org/10.1021/acs.jpcc.2c03804

75. Chen J-L, Kaltsoyannis N, DFT + U study of U_{1-y} An_yO_{2-x} (An = Np, Pu, Am and Cm) {111}, {110} and {100} surfaces, Appl. Surf. Sci., **537(5)** (2021) 147972. https://doi.org/10.1016/j.apsusc.2020.147972

76. Mccleskey TM, Bauer E, Jia Q, Burrell AK, et al., Optical band gap of NpO_2 and PuO_2 from optical absorbance of epitaxial films, J. Appl. Phys., **113(1)** (2013) 013515. https://doi.org/10.1063/1.4772595

77. Chen J-L. Theoretical study of actinide oxides [dissertation]. Manchester (United Kingdom): The University of Manchester; 2020. 246 p.

78. Cococcioni M, de Gironcoli S, Linear response approach to the calculation of the effective interaction parameters in the LDA+U method, Phys. Rev. B, **71** (2005) 035105. https://doi.org/10.1103/PhysRevB.71.035105

79. Qiu R, Ao B, Huang L, Effective Coulomb interaction in actinides from linear response approach, Comp. Mater. Sci., **171** (2020) 109270. https://doi.org/10.1016/j.commatsci.2019.109270

80. Aryasetiawan F, Imada M, Georges A, Kotliar G, Biermann S, Lichtenstein AI, Frequency-dependent local interactions and low-energy effective models from electronic

structure calculations, Phys. Rev. B, **70** (2004) 195104. https://doi.org/10.1103/PhysRevB.70.195104

81. Aryasetiawan F, Karlsson K, Jepsen O, Schönberger U, Calculations of Hubbard *U* from first-principles, Phys. Rev. B, **74** (2006) 125106. https://doi.org/10.1103/PhysRevB.74.125106

82. Gunnarsson O, Andersen OK, Jepsen O, Zaanen J, Density-functional calculation of the parameters in the Anderson model: application to Mn in CdTe, Phys. Rev. B, **39** (1989) 1708–1722. https://doi.org/10.1103/PhysRevB.39.1708

83. Anisimov VI, Gunnarsson O, Density-functional calculation of effective Coulomb interactions in metals, Phys. Rev. B, **43** (1991) 7570–7574. https://doi.org/10.1103/PhysRevB.43.7570

84. Sato A, Hada M, Abe M, Electron correlation effects on uranium isotope fractionation in U(VI)–U(VI) and U(IV)–U(VI) equilibrium isotopic exchange systems, Phys. Chem. Chem. Phys., **26** (2024) 15301–15315. https://doi.org/10.1039/d4cp01149j

85. Abe M, Suzuki T, Fuijj Y, Hada M, Hirao K, An *ab initio* molecular orbital study of the nuclear volume effects in uranium isotope fractionations, J. Chem. Phys., **129** (2008) 164309. https://doi.org/10.1063/1.2992616

86. van Stralen JNP, Visscher L, Larsen CV, Jensen HJA, First-order MP2 molecular properties in a relativistic framework, Chem. Phys., **311** (2005) 81–95. https://doi.org/10.1016/j.chemphys.2004.10.018

87. Møller C, Plesset MS, Note on an approximation treatment for many-electron systems, Phys. Rev., **46(7)** (1934) 618–622. https://doi.org/10.1103/PhysRev.46.618

88. Shamov GA, Schreckenbach G, Vo TN, A comparative relativistic DFT and ab initio study on the structure and thermodynamics of the oxofluorides of uranium(IV), (V) and (VI), Chemistry, **13(17)** (2007) 4932–4947. https://doi.org/10.1002/chem.200601244

89. Kovacs A, Molecular oxides of high-valent actinides, Struct. Chem., **31** (2020) 1247–1271. https://doi.org/10.1007/s11224-020-01555-3

90. Gueneau C, Chartier A, Van Brutzel L, 7.03–Thermodynamic and thermophysical properties of the actinide oxides, Comprehensive Nuclear Materials. 2nd ed., **7** (2020) 111–154. https://doi.org/10.1016/B978-0-12-803581-8.11786-2

91. Clavaguera-Sarrio C, Vallet V, Maynau D, Marsden CJ, Can density functional methods be used for open-shell actinide molecules? Comparison with multiconfigurational spin-orbit studies, J. Chem. Phys., **121** (2004) 5312–5321. https://doi.org/10.1063/1.1784412

92. Wen X-D, Martin RL, Scuseria GE, Rudin SP, Batista ER, A screened hybrid DFT study of actinide oxides, nitrides, and carbides, J. Phys. Chem. C, **117(25)** (2013) 13122–13128. https://doi.org/10.1021/jp403141t

93. Luo Z, Qin X, Wan L, Hu W, Yang J, Parallel implementation of large-scale linear scaling density functional theory calculations with numerical atomic orbitals in HONPAS, Front. Chem., **8** (2020) 589910. https://doi.org/10.3389/fchem.2020.589910

94. Mohr S, Ratcliff LE, Genovese L, Caliste D, et al., Accurate and efficient linear scaling DFT calculations with universal applicability, Phys. Chem. Chem. Phys., **17** (2015) 31360–31370. https://doi.org/10.1039/C5CP00437C